UC Irvine
UC Irvine Electronic Theses and Dissertations

Title
Shape Memory Polymer Micromachining for Wearable Sensors and Health Monitoring

Permalink
https://escholarship.org/uc/item/21d8j1th

Author
Pegan, Jonathan Dusan

Publication Date
2016

Peer reviewed|Thesis/dissertation

eScholarship.org Powered by the California Digital Library
University of California

UNIVERSITY OF CALIFORNIA,
IRVINE

Shape Memory Polymer Micromachining for Wearable Sensors and Health Monitoring

DISSERTATION

submitted in partial satisfaction of the requirements
for the degree of

DOCTOR OF PHILOSOPHY

in Engineering

by

Jonathan Dusan Pegan

Dissertation Committee:
Professor Michelle Khine, Chair
Professor Mark Bachman
Professor Abraham Lee

2016

Portion of Chapter 5 © Royal Society of Chemistry
Portion of Chapter 6 © Royal Society of Chemistry
All other materials © 2016 Jonathan Dusan Pegan

Dedication

To

My parents Daniel and Jan

&

My siblings Nicholas and Kendall

Table of Contents

Table of Figures v

Table of Tables vi

Acknowledgments vii

Curriculum Vitae viii

Abstract of the Dissertation x

1. Introduction 1

1. 1. Current state of wearable sensors 1

1. 2. Scalable manufacturing approaches 2

1.3 Overview of the dissertation 4

2. Shape Memory Polymers 5

2.1 Thermoplastic polyolefin shape memory polymers 5

2.2 Shape memory polymer mold fabrication 5

2.3 Shape memory polymers as the device substrate 6

3. Micromachining Methods 7

3.1 Overview of micromachining 7

3.1.1 Metal deposition principles and techniques 7

3.1.2 Etching principles and techniques 8

3.2 Lithography 9

3.2.1 Photolithography 10

3.2.2 Stencil lithography 11

4. Micromachining and Shape Memory Polymers Integration 11

4.1 General considerations 11

4.2 Metal deposition methods 12

4.3 Polymer etching methods 13

4.4 Lithography on polymers 13

5. Flexible High Surface Area Electrodes 14

5.1 Introduction 14

5.2 Experimental Design 17

5.2.1 Fabrication of shrunk electrodes 17

5.2.2 Electrode Design 18

5.2.3 Electrode characterization 18

5.2.4 Methods and principles of ECL detection 19

5.3 Results and discussion 21

5.3.1 Electrode characterization and performance 21
5.3.2 Multiplexed ECL detection using digital camera 23
5.4 Conclusions 27

6. Skin-Like Stretchable Strain Sensor 27
6.1 Introduction 27
6.2 Experimental Design 31
6.2.1 Fabrication of wPt strain sensors 31
6.2.2 Sheet resistance 32
6.2.3 Strain characterization 32
6.2.4 FEA modeling conditions 33
6.2.5 FFT parameters 33
6.2.6 Chest wall displacement sensor setup 33
6.3 Results and discussion 34
6.3.1 'Shrink' fabrication and transfer 34
6.3.2 Tunable strain sensors 35
6.3.3 Mechanism for tunable stretch sensitivity 41
6.3.4 Monitoring respiration 43
6.4 Conclusion 44

7. Future Directions 46
7.1 Transfer carrier materials and processing 46
7.1.1 Rapid Polymer Aging 46
7.1.2 Water soluble sacrificial layer 47
7.1.3 Chemically resistant polymers 47
7.2 Correlating sensor data with health parameters 48

References 49

Table of Figures

Figure 1 9
Figure 2 17
Figure 3 20
Figure 4 22
Figure 5 24
Figure 6 25
Figure 7 26
Figure 8 31
Figure 9 36
Figure 10 38
Figure 11 39
Figure 12 40
Figure 13 42
Figure 14 45
Figure 15 46

Table of Tables

Table 1 34
Table 2 44
Table 3 47

Acknowledgments

I would like to express my deepest gratitude to…

My family for providing love and support,

My friends for providing balance and perspective

My colleagues for providing ideas and inspiration

My Mentor, Michelle Khine, for continually challenging me to "*never settle.*"

Curriculum Vitae
Jonathan Dusan Pegan

EDUCATION

2009

Bachelors of Science in Biomedical Engineering

University of California, Merced

2013

Masters of Science in Biomedical Engineering

University of California, Irvine

2016

Doctorate of Philosophy in Engineering

University of California, Irvine

PUBLICATIONS

- **Pegan, J.**, Zhang, J., Chu, M., Nguyen, T., Park, S.J., Paul, A., Kim, J., Bachman, M., Khine, M. Skin-mountable Stretch Sensor for Wearable Health Monitoring. *Nanoscale* **39**, 17295-17303 (2016)
- Kim, J., Park S.J., Nguyen, T., Chu, M., **Pegan, J.**, Khine, M., Highly Stretchable Wrinkled Gold Thin Film Wires. *Appl. Phys. Lett*. **108**, (2016)
- Leser, M., **Pegan, J.**, Makkaoui, M.E., Schlatterer, J.C., Khine, M., Law, M., Brenowitz, M. Protein Footprinting by Pyrite Shrink-Wrap Laminate. *Lab Chip* **15**, 1645-50 (2015)
- **Pegan, J.**, Ho, A., Bachman, M., Khine, M. Flexible shrink-induced high surface area electrodes for electrochemiluminescent sensing, *Lab Chip* **13**, 4205-4209 (2013).
- Jayadev, S., **Pegan, J.**, Dyer, D., McLane, J., Lim, J. Khine, M. Adaptable wettability-enhanced surfaces ordered on molded substrates using shrink film. *Smart Mater. Struc.* **22**, 014014 (2013).
- Nguyen, D., McLane, J., Lew, V., **Pegan, J.**, Khine, M. Shrink-film microfluidic education modules: complete devices within minutes. *Biomicrofluidics* **5**, 022209 (2011).
- Nguyen, D., Sa, S., **Pegan, J.**, Rich, B., Xiang, G.X., McCloskey, K., Manilay, J., Khine, M. Tunable shrink-induced honeycomb microwell arrays for uniform embryoid bodies. *Lab Chip* **9**, 3383-3344 (2009).
- Grimes, A., Breslauer, D., Long, M., **Pegan, J.**, Lee, L. P., Khine, M. Shrinky-Dink microfluidics: rapid generation of deep and rounded patterns. *Lab Chip* **8**, 170-172 (2008).
- Chen, C.S., **Pegan, J.**, Luna, J., Xia, B., McCloskey, K., Chin, W.C., Khine, M. Shrinky-Dink hanging drops: a simple way to form and culture embryoid bodies. *J. Vis. Exp.* **13**, e692 (2008).

INTELETUAL PROPERTY

- US App. No. 62/000463, Flexible Strain Gauge for Fetal Movement Detection, *patent pending*
- US App. No. 62/000458, Flexible Sensor Apparatus, *patent pending*

PRESENTATIONS

- Wrinkled Metal Thin Film Sensors for Wearable Health Monitoring, SoCal Micro and Nanofluidics Symposium, Pasadena, CA 2015
- TinyKicks: Wearable Fetal Health Monitor, University of California system-wide biosymposium, Santa Cruz, CA 2015
- TinyKicks: *inutero* Fetal Health Monitoring, University of California system-wide biosymposium, Irvine, CA 2014
- Flexible high surface electrodes on plastic substrates for biosensing, IEEE EMBS Micro- and Nanoengineering in Medicine international conference, Maui, Hi, 2012
- High Surface area electrodes on flexible plastic substrates for integrated microfluidics, DARPA N/MEMS Science & Technology Fundamentals Program meeting, Irvine, CA, 2012
- Honeycomb microwell assay platform for generation and culture of embryoid bodies from human embryonic stem cells, Biomedical Engineering Society national conference, St. Louis, LA, 2008
- Quantitative single-cell analysis of receptor dynamics and chemotactic response on a chip, Biomedical Engineering Society 2007 national conference, Los Angeles, CA, 2007
- Quantitative single-cell analysis of receptor dynamics and chemotactic response on a chip, University of California system-wide biosymposium, San Francisco, CA, 2007

AWARDS & HONORS

- UC Business Plan Competition People's Choice Award, University of California system-wide biosymposium, 2015
- BioAccel business plan competition winner with $75k investment, 2015
- Honorable mention, National Science Foundation Graduate Research Fellowship Program, 2012
- Honorable mention, National Science Foundation Graduate Research Fellowship Program, 2011
- 3rd place poster winner, Campus-wide undergraduate research competition, University of California, Merced, 2009
- 1st place poster winner, Campus-wide undergraduate research competition, University of California, Merced, 2007
- Elected to Sigma Xi honor society, 2007
- 1st place poster winner, National Science Foundation COINS undergraduate fellow research competition, University of California, Berkeley, 2006
- 3 time National Science Foundation competitive summer undergraduate research fellow University of California, Berkeley/Merced, 2006, 2007, 2009

Abstract of the Dissertation

Shape Memory Polymer Micromachining for Wearable Sensors and Health Monitoring

By Jonathan Dusan Pegan
Doctor of Philosophy in Engineering
University of California, Irvine, 2016
Professor Michelle Khine, Chair

Despite many advances in mobile communications and data science remote, continuous health monitoring remains a challenge due to a dearth of appropriate wearable sensors. These sensors must bend and stretch along with the human body while maintaining consistent performance. As most standard electronics component are made of rigid, brittle materials, there is an inherent mechanical mismatch that limits the usefulness of current sensor technology for wearable health monitoring.

This work introduces pre-stressed thermoplastic shape memory polymers as a fabrication tool to produce complex, hierarchically wrinkled thin films for use as wearable sensing electrodes and wearable strain sensors. Additionally, a series of scalable, polymer compatible micromachining techniques are discussed for fabricating these sensors.

Hierarchical wrinkled structures significantly enhance the surface area (>600%) as compared to planar thin films. Integrated with a flexible polymer carrier, wrinkled electrodes can provide increased efficiency with low sample volumes for electrochemical sensing on human skin. This enables potential application of bioanalyte detection in human sweat.

Out of plane wrinkling in thin films can also serve as a strain relief. By transferring wrinkled metal thin films into an elastic carrier, highly elastic strain sensors can be fabricated and used to detect and monitor human motion. These sensors show very high gauge factors (as high as

42) over a wide dynamic range (>150%). Worn on the chest, these sensors can monitor breath rate and approximate lung volume based on chest wall displacement as is demonstrated in this work.

Finally, future work with possibility of incorporating a water soluble sacrificial layer are discussed. The addition of hydrophilic polymers as a lift off layer increases flexibility and ease of transferring wrinkled thin films. Importantly water-based processing would convert the current solvent-base lift off process to a more green manufacturing process.

1. Introduction

1.1 Current state of wearable sensors

The "Internet of Things" (IoT) revolution has been enabled by advances in mobile communications and data science; yet, many applications currently remain out of reach due to limitations in available sensor technology. For example, advances in mobile health (mHealth) monitoring has been stymied by a lack of available conformal sensors.[1–3] Wearable devices have seen some early success by packaging standard and/or flexible electronics to be adorned as "smart" fashion accessories for consumers. However, such sensor technology remains unable to produce accurate, quantitative biometric data to be usable for many mHealth applications.[1,4]

Many of the early successes in wearable electronics, such as fitbit, have relied on accelerometers as sensors. As such, many research studies have focused on clever placement of off the shelf accelerometers on the body. Due to their small size and high sensitivity they can be placed somewhat unobtrusively onto the human body. With the addition of implementing sophisticated algorithms classification of gait,[5] respiration,[6] and even fetal movement has been performed.[7] However, discernment of precision movement and extraction of signal from noise remains challenging with accelerometers alone. [1,8] For this reason, biometric data from an abundance of commercially available wearable devices are often reduced to less specific quantitative measurements such as "activity."[1,8,9]

Current efforts in designing new wearable sensor can be separated primarily into two materials based approaches: metals[10–16] and carbon.[17–24] Metallic materials benefit from intrinsically good conductivity and an established infrastructure for deposition and micromachining of high quality thin films. However, due to the extreme mechanical mismatch of metals and human skin, thin films and mechanical optimization are required in order to lower the

effective modulus and reduce strain in the material, respectively. Carbon materials, such as carbon nanotubes (CNTs) and graphene cope with the high strain present on the human body well. However, electrical properties depend heavily on processing[25] and biocompatibility of nanoparticles is relatively unknown.

As future scale of manufacturing is considered heavily for the devices presented in this work, the ability to leveraging existing integrated circuits (IC) and microelectromechanical systems (MEMS) processing infrastructure to produce consistent, high quality conductive thin films is advantageous. Therefore metal thin films are selected for each of the wearable sensors presented in this work. Other materials considerations outside of processing are further discussed in later chapters which identify metals as ideal conductors for the presented sensors.

1.2 Scalable manufacturing approaches

Micromachining and manufacturing techniques heavily influenced the development and availability of many of today's technologies. This is of particular importance in rapidly developing areas of wearable sensors research. Progress in the way of manufacturing techniques enables researchers with more tools and capabilities for innovating the next generation of wearable sensors. Riding the success of the IC and MEMS industries, there has been a rapidly growing interest in sensor development for mHealth applications.[26] At the vanguard of this budding research area is flexible electronics.[1,9,27,28] In this field electronic components, often sensors, are adapted for use on the human body. Customarily rigid and planar electronics are redesigned in soft materials to stretch and contour with the human body. Of particular interest is the potential of such electronic wearable systems for remote, continuous health monitoring.[1,26,27] Successful integration of wearable technologies into mHealth networks would increase the access to health care to lower resource and/or remote regions where hospitals may be scarce.[29]

There exist many challenges with current wearable sensor technology that hinders these devices from reaching users and patients. There is a major gap between research and development, and manufacturing of these devices into products. Primarily, devices are made during development with very little consideration of scalable manufacturing techniques. As many of the current methods for fabricating commercial wearable devices have been repurposed MEMS devices such as accelerometers, with the primary material substrate is ultrathin silicon.[8,30–32] These rigid materials are often not optimal for long-term health monitoring applications.[33] Additionally, the miniaturization of flexible electronics is many magnitudes less than the scale of current integrated circuits. Therefore the scalability of wearable devices constrained to wafer-based fabrication methods are limited.

Fabrication in the research and development phase is often done using serial processes, which are difficult to scale for high throughput production. Methods for making these devices often involve many manual techniques performed by individual researchers. Significant additional resources and time is often needed to then rework the fabrication scheme to efficiently manufacture these devices. By incorporating scalable fabrication techniques into the initial design of the wearable components, translation can be more easily accomplished.

Being that many of the current microfabrication techniques are borrowed from the IC and MEMS common electronic materials tend to be hard, planar, and rigid, while most biological systems are soft, curvilinear, and flexible. This mechanical mismatch leads to poor biocompatibility.[33] Moreover, substrates for device fabrication such as glass and silicon also have relatively small finite surface area, limiting processing to either serial, or low yield batch processes.[34] Therefore these materials are inherently restricted in scalable manufacturing

capabilities. New, more biocompatible materials that are more easily adapted to scalable manufacturing methods must be realized for improved success in translating wearable sensors.

1.3 Overview of the dissertation

To address the aforementioned hurdles in effectively designing, fabricating, and translating biomedical wearable sensor technology, this work presents processing techniques for scalable manufacturing of wearable sensors based around inexpensive polymers. Micromachining techniques invented for mass manufacturing in the IC and MEMS industries can be utilized in a way that is amenable to scalable production for wearable electronics. However, wafer-based design principles do not apply to wearable sensors that have inherently larger footprints and generally adopt modular designs.[35] In chapter 2, shape memory polymers (SMPs) and their use as a fabrication tool is introduced. In chapter 3, common micromachining techniques are discussed and in chapter 4 these techniques are adapted to be compatible with low cost, SMP films. Chapter 5 more finely discusses how scalable fabrication techniques are used to demonstrate electronic integration of flexible SMPs with wrinkled metal thin film electrodes for potential bioanalyte detection on the body. Chapter 6 builds on the electrode work by transferring these wrinkled metal thin films into elastic polymer films for the fabrication of skin-like strain sensors. A proof of concept experiment for wearable breath monitoring in demonstrated and discusses as well. Chapter 7 concludes with some speculation on future directions for this research to enable more successful translation of wearables sensors for health monitoring.

2. Shape Memory Polymers

2.1 Thermoplastic polyolefin shape memory polymers

SMPs are polymer materials that have the ability to return from a temporary state (or shape) to an original, permanent state when the correct external stimuli is given. [36] This work utilizes two thermoplastic SMP films: polystyrene (PS) (Grafix, Shrink Film) and a proprietary polypropylene/polyethylene laminate (Sealed Air, 955D), heretofore referred to as polyolefin (PO). These films are pre-stressed (temporary state) and shrink to a smaller size (permanent state) when heated above the glass transition temperature (T_g) of the polymer. In brief, the permanent shape of the polymer is defined by a higher temperature phase than T_g which forms crosslinks in the polymer network. The shape memory is programed utilizing the lower temperature phase above T_g and below the permanent temperature threshold. At T_g individual polymer chains which naturally reside in a coiled state soften. Once at T_g, the films are extruded (or stressed) which stretches these softened polymer chains. While stressed the SMPs are cooled, the soft polymer chains in the network harden, holding the polymer in the temporary state. These chains soften again and coil up when heated past T_g allowing the film to shrink to it's original, permanent shape. The PS and PO films used in this work have similar T_g at 125 ºC and 100 ºC, respectively. The polymers PS and PO shrink by 67% and 95% by area, respectively. More specifically, the pre-stresses SMPs grow in the z-direction as the polymer shrinks in the xy-plane. This can concentrate or compresses materials strongly adhered to the surface of the SMP.

2.2 Shape memory polymer mold fabrication

Previous work has utilized this ability to compress patterned materials on the SMP surface to make higher aspect ratio, rounded channels for microfluidic prototyping.[37–39] Printer toner was deposited directly onto the SMP and subsequently shrunken to form a mold for rounded

microfluidic prototyping without the need for cleanroom facilities. A similar approach is used to create custom microwell arrays for embryoid body formation.[40] Rigid materials such as oxide films and metal films can be used to create complex, hierarchical wrinkled surfaces.[41–44] These rough wrinkled surfaces can then be molded[42] or embossed[41,43,45] into a variety of polymers substrates. Consistent with the Cassie-Baxter model,[46] these roughened surfaces enhance the intrinsic hydrophobicity of low surface energy polymers to become superhydrophobic.[41–43,45] Importantly, this method for creating complex wrinkled surfaces has been shown to integrate well with roll-to-roll manufacturing schemes.[45]

2.3 Shape memory polymers as the device substrate

The complex wrinkled structures created by applying a rigid thin film on top of SMPs can also produce very high area surfaces. These high surface areas can be useful for increasing reaction rates,[47–49] creating optical scattering surfaces,[50,51] and many other surface applications. Leser *et al.* demonstrates increase efficiency of reactions to great effect using high surface area pyrite nanocrystal coated SMP surfaces to generate sufficient OH for oxidative footprinting analysis of proteins in 4µL samples.[48] With similarly high surface area hierarchical silica surfaces on SMPs Lin *et al.* showed >100x enhancement of light intensity from surface immobilized fluorescent biomolecules over similar studies on glass.[50] This work builds on this method for creating high surface area surfaces for electrochemical applications suitable for wearable bioanalyte detection in chapter 5. In chapter 6 the usefulness of SMPs in microfabrication is further extended by transferring wrinkled thin films created on SMP carriers into elastic, skin-like polymers for wearable breath monitoring.

3. Micromachining Methods

3.1 Overview of micromachining

Micromachining includes a vast array of different fabrication techniques, both additive and subtractive. Additive techniques involve deposition of materials onto a substrate. In contrast, subtractive techniques involve removing materials from a layer or bulk substrate. Processes included in this work relate to metal deposition (additive) and etching (subtractive).

3.1.1 Metal deposition principles and techniques

The deposition of metal thin films is performed using two primary processes: sputtering and evaporation. Sputter deposition is a physical vapor deposition process that involves ejecting atoms from a target material and depositing them into a sample substrate. Evaporation is a process in which the target material is heated past the evaporation temperature to create a vapor that condenses onto a sample substrate.

Sputtering tends to be a serial process with more uneven film deposition and lower purity due a lower vacuum pressure as necessitated by the need for gas molecules, usually argon, to be present during operation[52]. These Ar molecules fill the space between parallel electrodes which create a large electric field inside the sputter chamber. Due to random thermal collisions between the Ar molecules free electrons and Ar+ are created. These charged particles, accelerated by the electric field, collide with other Ar molecules to create a chain reaction of ionization creating plasma. The Ar+ bombards the material target, often a noble metal such as gold, placed at the cathode. Small clusters are physically knocked from the target, which impact and deposit onto the sample substrate at the anode. This process is generally performed at room temperatures with very little sample heating. This makes for an ideal process for metal deposition onto temperature

sensitive SMP samples at the aforementioned cost of somewhat low film quality and serial sample loading.

In contrast to the serial nature of sputter deposition, Evaporation systems are more commonly equipped with large sample chamber which accommodate multiple substrates that are processed in parallel. Film quality is also very high due to very high vacuum pressures that are needed inside the deposition chamber. Evaporation is a physical vapor deposition process in which the target material is placed in a boat, and heated in a vacuum past its evaporation temperature to create a vapor. The heating element of these systems can vary. Typically a high electrical current thermoresistor is used as a heat source. In the case of this work, a focused electron beam (ebeam) is used to heat the target as this technique keeps sample temperatures low. The vapors from the target material condensates onto the desired substrate material placed at the top of the chamber.[52] The vapor cools upon contact adhering to the surface of the substrate forming a thin layer.

3.1.2 Etching principles and techniques

Etching is a subtractive technique were material is removed from a layer, or the bulk substrate to form features. Specifically, wet etching is a process in which a substrate is immersed in a chemical solution bath that will dissolve the material to be removed. This simple procedure is inexpensive, has a high etch rate, and has good specificity for most materials. However, the disadvantage lies in the possibility of dissolving underneath the mask on top of the substrate used to define the features. Depending on the substrate material, wet etching can yield different etching profiles, either isotropic or anisotropic[52]. Isotropic etching profiles have equal etch rates in all directions. This etching profile can cause under etching of the mask and rounded corners (Figure 1A). Anisotropic etching is based on the orientation of the substrate being etched. This etching profile has different etch rates along the horizontal and vertical axis making high aspect ratio

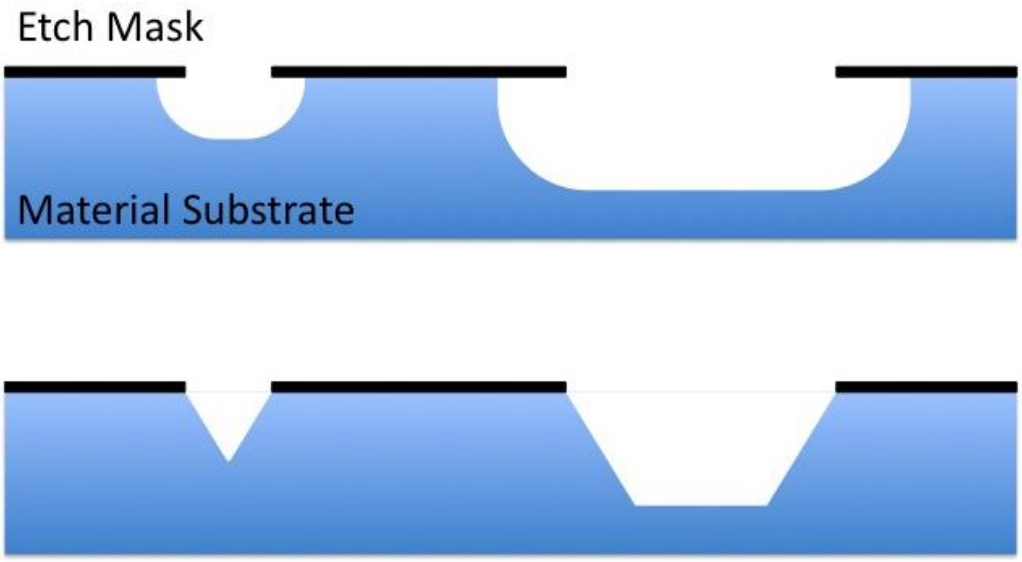

Figure 1 illustration of isotropic (top) and anisotropic (bottom) wet etch profiles in crystalline materials

channels possible (Figure 1B). This type of etching profile is more common in dry etching processes.

For this work a variety of wet etching processes are used depending on the material substrate. For patterning Au thin films on SMPs discussed later in aim 1, potassium iodide (KI) (1:4:40 I_2/KI/H_2O) solution was used as a Au etchant. For performing PS lift-off as discussed in aim 2, a combination of organic solvents are used to etch away a PS support layer. For performing a lift-off later discussed in aim 3, water will be used to etch away a water soluble sacrificial layer.

3.2 Lithography

Lithography is a common microfabrication technique transferring a two-dimensional (2D) pattern from a physical mask or template onto a sample substrate. Photolithographic processes utilizes photosensitive polymer, or photoresist, spin coated onto a substrate to transfer patterns or geometric shapes from a photomask, typically via UV light. Stencil lithography utilizes a shadow

mask with the pattern or geometric shapes cut out of the physical sheet allowing materials or etchants to pass through onto the sample substrate.

3.2.1 Photolithography

The photolithography process traditionally includes spinning a viscous photoresist onto a flat, rigid substrate, usually a silicon (Si) wafer. The wafer is then put through a baking step to evaporate the solvents in the photoresist and promote good adhesion of the photoresist layer to the Si substrate. A photomask is used to define the desired 2D geometry. Typically this mask is put in contact over the photoresist layer and then exposed to UV light of wavelength ranging between 150nm to 300nm for a few seconds[52]. A post exposure bake is sometimes necessary depending on the type of photoresist to drive the reactions initiated during the UV exposure to completion. Faint images in the photoresist seen from the exposure process are defined in 3D when the wafer is developed in a solvent bath. A post process hard bake is often employed increasing the photoresist layer's hardness and adhesion to the Si substrate.

Photoresist comes in two different tones: positive and negative. Positive resist tones give an exact copy of the photomask after development. This is because exposure to UV light causes cleaving of the polymer chains in the photoresist making them easier to dissolve away during development. Negative resist tones are the opposite in nature. They produce the inverse image of the photomask. Polymerization, or cross-linking of the polymer chains occurs during exposure to UV light; therefore resisting dissolving in developer solution. The photomask used for these resist tones are of the negative image of the desired final design.

There are two primary types of photomasks: Chrome masks and transparencies. Chrome masks are made by depositing a thick layer of chrome onto a quartz sheet. The desired pattern is then etched into the chrome layer by ebeam (10nm resolution) or laser ablation (500nm

resolution)[53]. This process requires expensive clean room facilities and the cost per mask typically ranges $200-$800. Alternatively transparencies are much cheaper ($15-$150) but are limited in resolution to approximately 8μm. High-resolution laser printers are used to deposit toner in the desired pattern onto Mylar transparency films.

3.2.2 Stencil lithography

Stencil lithography offers a rapid and inexpensive alternative to photolithography when high resolution is not required. Cut outs are made in a thin material to act as a shadow mask so that when placed over a samples substrate, materials are only deposited through those cut outs. Shadow mask are most commonly made by laser machining. Resolution in this depends primarily on the mask material and excitation source of the laser. For this work, a CO_2 laser is used to machine 25 μm thick polypropylene sheets. Due to the relatively long wavelength of the laser and the heat susceptibility of the polymer film the resolution is limited to 50 μm.

4. Micromachining and Shape Memory Polymers Integration

4.1 General considerations

Wearable integration of electronics requires new materials that can cope with mechanical strain, moisture, and temperature gradients not normally present in standard electronics applications. Softer materials such as polymers have been found to perform well for wearable applications in part by reducing the mechanical mismatch between sensor components and human skin.[13,20,28,54] However, these materials introduce processing constraints when integrating into MEMS and semiconductor microfabrication tools. The two most critical constraints with respect to this work are sensitivity to heat and chemical susceptibility. Processing with SMPs must remain

below the T_g of the polymer until miniaturization of the film is desired. Thermoplastic SMPs are also generally sensitive to chemical solvents. However, the degree of susceptibility depends on the polymer. PO films utilized in this work are highly resistant, although some swelling may occur, to organic solvents whereas PS is extremely soluble by comparison. Micromachining and lithography techniques are discussed in this chapter with special consideration of these aforementioned processing constraints of SMPs.

4.2 Metal deposition methods

Deposition of metals onto polymers differs from Si processes due to temperature constraints and the growth dynamics of the metal film. Specifically to PS and PO SMPs, the processing temperature threshold is the T_g of the polymer (125 ºC and 100 ºC, respectively). Due to the low surface energy of these polymers and limited formation of surface oxides, thin metal films tend to contain more discontinuities and adhesion is often very poor.[55] However, low temperature physical vapor deposition methods such as sputter deposition and ebeam evaporation can produce high quality metal thin films on SMPs.

Sputter deposition processes typically operate below 100 ºC depending on desired film thickness or deposition time. For thicker films, the deposition can be split into multiple steps, allowing for the sample to cool between each step. Film adhesion is good with few discontinuities once films reach a confluent thickness due to high energy metal ion clusters physically bombarding the polymer film and oxygen plasma generation during sputtering.[55,56]

Operation temperatures of ebeam evaporation are generally well below 100 ºC due to the heat required for metal vaporization being highly concentrated at the target surface incident with the ebeam. In addition sample cooling is often available in order to provide finer tuning of vapor condensation rates on the substrate surface. ebeam evaporation delivers a very high quality film

due to the high vacuums required for operation. Low chamber pressure removes possible contaminates such as oxidation agents and metal vapors condense on the SMP surface with less shadowing effect from physical masks. However, due to the low surface energy of SMPs some discontinuities in the thin film appear and adhesion to the SMP surface is low.[55] Adhesion can be improved by oxygen plasma ashing prior to deposition.[56] However, due to relatively poor adhesion films are generally limited to 50 nm before internal stresses in the film can cause delamination from the SMP substrate.[57]

4.3 Polymer etching methods

SMPs are compatible with both wet and dry etching processes. However, unlike crystalline materials SMP have an amorphous structure. Therefore, anisotropic etching profiles are unattainable in wet etching processes. Isotropic etch rates depend on monomer chemical composition and etchant.[58] Organic polymers such as PS are very susceptible to more aggressive organic solvents such as acetone and toluene. In contrast, PO has very good chemical resistance. Therefore, dry etching methods are preferred when working with PO such oxygen plasma etching as demonstrated by Jayadev *et al*.[42] As mentioned in chapter 3, dry plasma etching is 'line of sight' and therefore achieves an anisotropic etching profile. This method is also suitable with PS.

4.4 Lithography on polymers

Lithography is paramount for defining the high resolution geometries of electronic components. Special considerations must be made when working with particular SMPs in order to achieve good fidelity between the mask and device material.

Between the two lithography methods discussed in chapter 3, photolithography provides the highest resolution. However, due to organic solvents present in the resist tones, PS is not a compatible materials for photolithography. PO has excellent chemical resistance and copes with

resists,[42,49] developers, and chemical wash processes well. Many 'standard' photolithography processes often call for baking the substrate near 100 ºC, the T_g of PO. These processes must be modified in order to prevent premature miniaturization of the PO substrate before all other processing steps are complete. Often lower baking temperatures for longer durations can achieve the desired results.

Stencil lithography does not require high heat or chemical contact with the carrier SMP. If high resolution is not required, stencil lithography is a viable alternative to photolithography. Since SMPs are well known for their ability to decrease patterned feature sizes as introduced in chapter 2,[38,39] the resolution limits of stencil lithography can be surmounted by utilizing SMP processing. Stencil lithography is especially ideal for polymers with low chemical resistance such as PS.

5. Flexible High Surface Area Electrodes

5.1 Introduction

Simple, robust, and affordable medical diagnostics that deliver rapid, sensitive results at the point of care (POC) would provide otherwise unavailable healthcare to developing regions.[29,59] Lab-on-a-chip (LOC) technologies, which have the ability to probe minute fluid volumes holds particular promise for this need with inherent advantages such as portability, rapid reaction times, and low required reagent volumes.[29,59–61] However, there have been relatively few success stories of microfluidic devices being utilized in such regions to date.[61,62] One of the fundamental barriers responsible for this is an over reliance on external, dedicated laboratory equipment needed to interface with many microfluidic devices. Microfluidic devices then become a component of an otherwise complex, expensive, non-portable system ill-suited for the POC environment.[59,61] Leveraging the massive connectivity of current mobile technology and taking microfluidic

measurements at the source on the skin with wearable sensors could relieve microfluidic systems for relying on laboratory resources.

While paper based microfluidics obviates some of these issues, they are inherently limited from detecting low concentrations, with typical detection ranges of mM to tens of μM.[63,64] Koh *et al.* successfully demonstrated an on-skin paper microfluidic system to sample a user's sweat over time. Importantly, however, because colorimetric results are heavily influenced by ambient light these tests are limited in their quantitative ability and offer mostly qualitative, positive/negative conclusions.

Electrochemistry is an extremely sensitive mode of detection. Important biomolecule concentrations such as glucose,[65,66] lactic acid,[66] and uric acid,[67] and cortisol[68] have been successfully quantified at low concentrations, some as low as fM, utilizing laboratory grade apparatus. Electrochemical detection schemes are also easily miniaturized making them attractive for POC applications. Eletrochemiluminescence (ECL), where electro-generated species combine to convert electrochemical energy into radiative energy, has become increasingly relevant for POC applications as it combines the advantages of both electrochemistry and chemiluminescence. Tris(2,2'-bipyridyl)ruthenium(II) ($Ru(bpy)_3^{2+}$) and its many coreactants that react with the oxidized form of $Ru(bpy)_3^{2+}$ to emit light, is one of the most widely utilized ECL complexes in biomedical analytical devices.[69–71] Biomolecules can be easily labeled with $Ru(bpy)_3^{2+}$ for immunoassay, magnetic bead, and DNA-based detection schemes.[69] $Ru(bpy)_3^{2+}$-based ECL has inherent advantages such as extreme stability, high sensitivity, low detection limit, wide dynamic range, ability to link with a wide range of analytes, excellent spatial and temporal control, good water solubility, and compatibility with separation techniques. Unlike colorimetric assays, ECL experiments are independent of ambient light. Delaney *et al.* was the first to show successful ECL

detection of nicotinamide adenine dinucleotide (NADH) and 2-(dibutylamino)-ethanol (DBAE) in a microfluidic paper-based electrochemical device (μPED).[72] Importantly, this work also demonstrated good portability and compatibility with mHealth networks, with ECL detection carried out using a cell phone camera. Ge *et al.* expanded the utility of ECL μPEDs by developing a multiplexed sandwich type assay.[64] Sardesai *et al.* recently showed microfluidic ECL with 10-25 fold enhancement in detection limits over non-microfluidic arrays.[73] These aforementioned studies all represent important milestones in the development of ECL for POC and/or mHealth.

An integrated, flexible plastic ECL sensor using shape-memory PO film as a wearable sensor could deliver efficient bioanalyte sensing on the body. To date, these pre-stressed PO films have been used for creating many biomedical devices.[37,40,44,60,74] This is the first demonstration of shrink electrode integration using a standard microfabrication approach. This method utilizes low cost, roll-to-roll compatible plastic and integration with well-established integrated circuit (IC) and microelectromechanical systems (MEMS) infrastructure; this enables a cost-effective, scalable manufacturing scheme capable of high resolution. Open-face design leveraging our superhydrophobic (SH) surfaces allows for easy spotting of reagents that remained confined to detection zones without the need for expensive external pumps.[42] This surface tension controlled ability to manipulate liquid also lends itself to the possibility of multiplexing by integrating multiple samples on a single chip. Integration with microfluidics is also possible as the Khine Group has previously demonstrated these thermoplastics are an excellent material for such applications.[74,75] Importantly, samples can be easily reclaimed for subsequent analysis or storage. Inherent in shrink fabrication is the ability to create high surface area 'wrinkle' structures.[47,76,77] When applied to metal thin films, high surface area electrodes can be simply fabricated,[47,77] dramatically improving speed and performance of electrochemical sensors.[78,79] Importantly, with

the added 20-fold increase in resolution from shrinking on a PO substrate, significantly higher resolution electrodes are created over photolithographic patterning on planar surfaces alone as well as to previously published shrink-induced electrodes.[47,77]

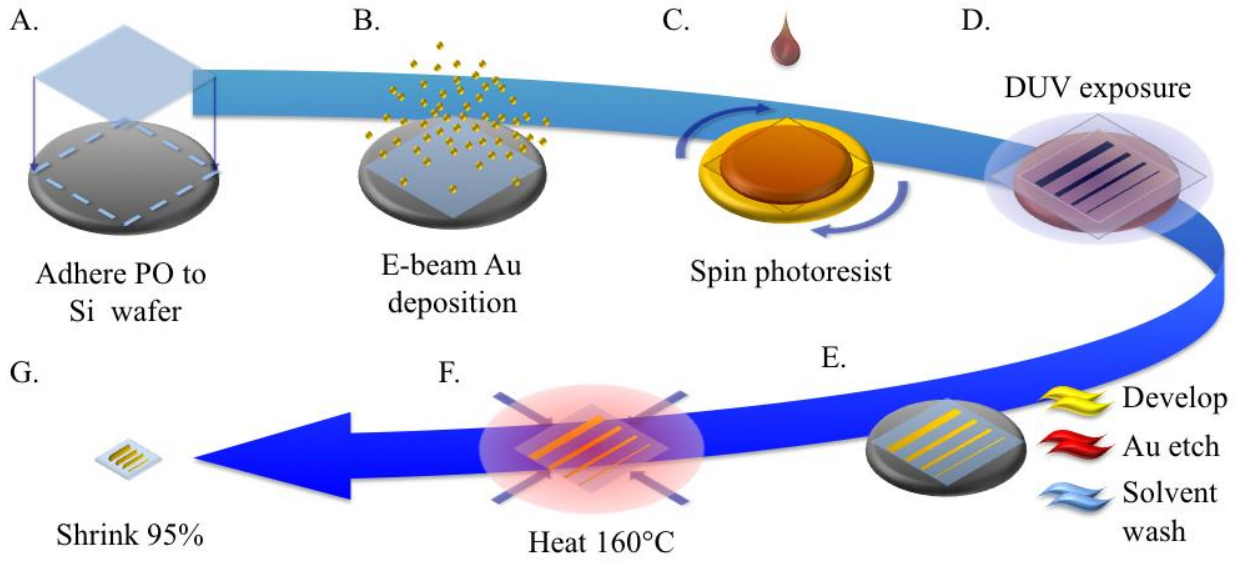

Figure 2 fabrication process flow. A. PO is adhered to a Si wafer support, B., 40 nm is e-beam deposited, C., photoresist is spun onto the Au coated sample. D. The sample is exposed with a photomask to define electrode features. E. The sample is then developed, submerged in Au etchant, and cleaned with a solvent wash to produce Au patterned electrodes. F. The sample is then heated, G., to shrink the device footprint by 95%.

5.2 Experimental Design

5.2.1 Fabrication of shrunk electrodes

PO films were affixed to Si wafers using DIH_2O to provide mechanical support for compatibility with standard micromachining equipment. Characterization of the PO film properties and reproducibility have been previously reported.[38] A 40 nm Au thin film was deposited by ebeam evaporation (Temescal CV-8). The Au coated PO film then underwent a photolithography and wet etching process for patterning of the desired electrode design (Figure 2).

In this two-part process Shipley 1827 photoresist (Microchem, MA) was patterned using a photomask and DUV flood hood (ABM, CA). After development of the sample, the remaining photoresist acted as a protective barrier against the I_2:KI:H_2O (1:4:40) Au etchant. The photoresist layer was removed using acetone. Patterned Au and PO films were then lifted from their Si wafer supports and heated past the PO T_g using a commercial heat gun (Steinel HL1820S), shrinking the patterned electrodes by 95% within seconds[38,42] (Figure 3A-C). Alternatively, wet etching can be avoided by patterning photoresist on the bare PO films prior to Au deposition with subsequent lift off to create Au-free regions between electrodes. Otherwise, all processing steps remain the same.

5.2.2 Electrode Design

Electrode designs were drawn using CAD software (Autodesk, Inc., CA). For designs that demanded higher resolution, CAD drawings were sent out to be printed on transparencies (Fineline Imaging, CO). Electrode line widths of 4 μm were achieved after completing the thermal shrinking process using these printed Mylar photomasks. Alternatively, photomasks were laser machined in house from PMMA using a bench top laser cutter (VLS2.30, Universal Laser Systems, AZ). Utilizing the faster turn-around time of this method, devices could go from design to fabricated device within a few hours.

5.2.3 Electrode characterization

The electrical resistivity and electrochemically active surface area of the Au thin film electrodes were quantified before and after the shrinking process. A 4-point measurement method was performed to determine resistivity of the Au thin films. In short, a constant current is applied (E3611A, Agilent, CA) to individual Au thin film traces of different widths while voltage is recorded (117 Multimeter, Fluke, WA) to accurately measure resistance. Cyclic voltammetry was used to determine the electrochemically active surface area of the Au thin film electrodes as

outlined by Gabardo *et al.*[47]. Briefly, a three-electrode electrochemical cell was setup with Ag/AgCl reference electrode (SPE, TX), Pt counter electrode (Sigma Aldrich, MO), and a Au thin film on PO serving as the working electrode. These three electrodes were submerged in 0.1mM H_2SO_4 (Sigma Aldrich, MO) while electric potential was cycled between -0.1 – 1.5 V at a scan rate of 20 mVs^{-1} for 4 cycles (model DY2013 potentiostat). The electrochemical activity of the Au thin film electrodes was measured using the 4th cycle.

5.2.4 Methods and principles of ECL detection

$Ru(bpy)_3^{2+}$ and DBAE (Sigma Aldrich, MO) coreactant was chosen as this system is well understood.[80] 2 μL mixtures of both reagents (1:1) were spotted onto 15 separate detection zones for each sensor. A dilution of DBAE (5000 – 5 μM) was tested in triplicate on a single sensor while $Ru(bpy)_3^{2+}$ concentration (5000 μM) was kept constant at each detection zone. All reagents for ECL were suspended in 0.1 mM PBS (Sigma Aldrich, MO) unless otherwise stated. Patterned Au thin films constituted the working electrode while a transparent ITO coated glass microscope slide served as both the counter electrode as well as a top-sheet, enclosing the electrochemical cell when placed over the droplets. A PMMA spacer layer was used to hold the ITO counter electrode 1 mm above the ECL sensor so that contact was made with the droplet samples, but not the Au thin film electrodes. ECL was excited by applying 2.1V from a bench top power source (E3611A, Agilent, CA). Notably, for POC applications a quick 1sec pulse from a battery could used. Multiplexed ECL detection was carried out using a CMOS sensor from a consumer camera (Rebel Ti3, Canon, CA) positioned above the ITO counter electrode. Luminescent intensity was integrated over 1 sec using the CMOS sensor at 1600 ISO sensitivity and the resulting images were analysed

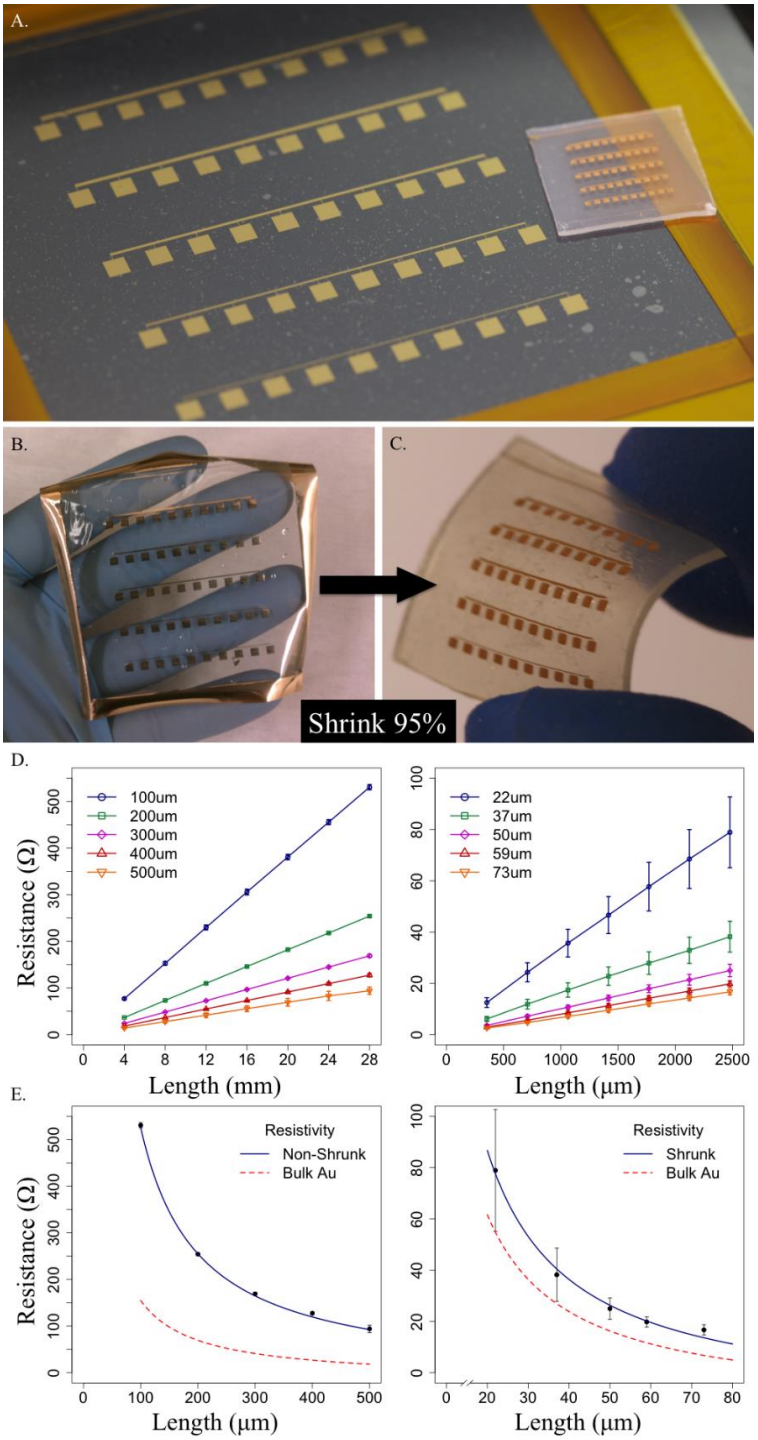

Figure 3 Patterned Au thin film electrodes. A. before (left) and after (right) thermal shrinking, B. Patterned electrodes, C., remain flexible after the shrinking process. D. 4 pt measurements of non-shrunk (left) and shrunk (right) electrodes show lower resistance. E. Resistivity of the 40 nm thin film electrodes is decreased for shrunk electrodes, modeled with regression coefficient to correct systematic error from empirical measurements.

using ImageJ software.[81] Five different devices for each condition were tested.

5.3 Results and discussion

5.3.1 Electrode characterization and performance

Upon heating above the glass T_g of PO, the stiffness mismatch between the two materials causes the Au thin film to buckle from the compressive stress of the shrinking polymer.[47,77] Notably, robust integration of the Au thin film with the PO film occurs during this process (withstanding microfluidic flow,[75] repeated molding[41] without delamination). The PO partially reflows at high temperatures, increasing adhesion to the thin film without the need for adhesion layers between the polymer and Au. The resulting micro- and nano-wrinkling of the Au thin film is responsible for improved electrical performance, characterized by improved electrical resistivity.

4 pt measurments of non-shrunk and shrunk electrodes show that both have a linear decrease in resistance across patterned line electrodes of different widths (Figure 3D). Measuring electrical resistivity before and after the thermal shrinking process shows a dramatic improvement of the wrinkled Au thin film electrodes (0.033 Ω*μm) over the non-shrunk, planar Au electrodes (0.077 Ω*μm). Notably, the effective resistivity of the 40 nm wrinkled Au thin film begins to approach bulk Au resistivity (0.024 Ω*μm) (Figure 3E). This decrease in electrical impedance is therefore not simply an effect of reducing the mean path of resistance due to the smaller shape of the polymer. Cross-sections of the wrinkled Au thin films reveals many tens of micron-scale invaginations in the surface where adjacent wrinkles pack closely enough that they begin to coalesce, referred to as secondary folding.[47] In a flat Au thin film, discontinuities produce a large effect in the resistivity of the film.[82] I hypothesize that secondary folding in the wrinkled Au thin

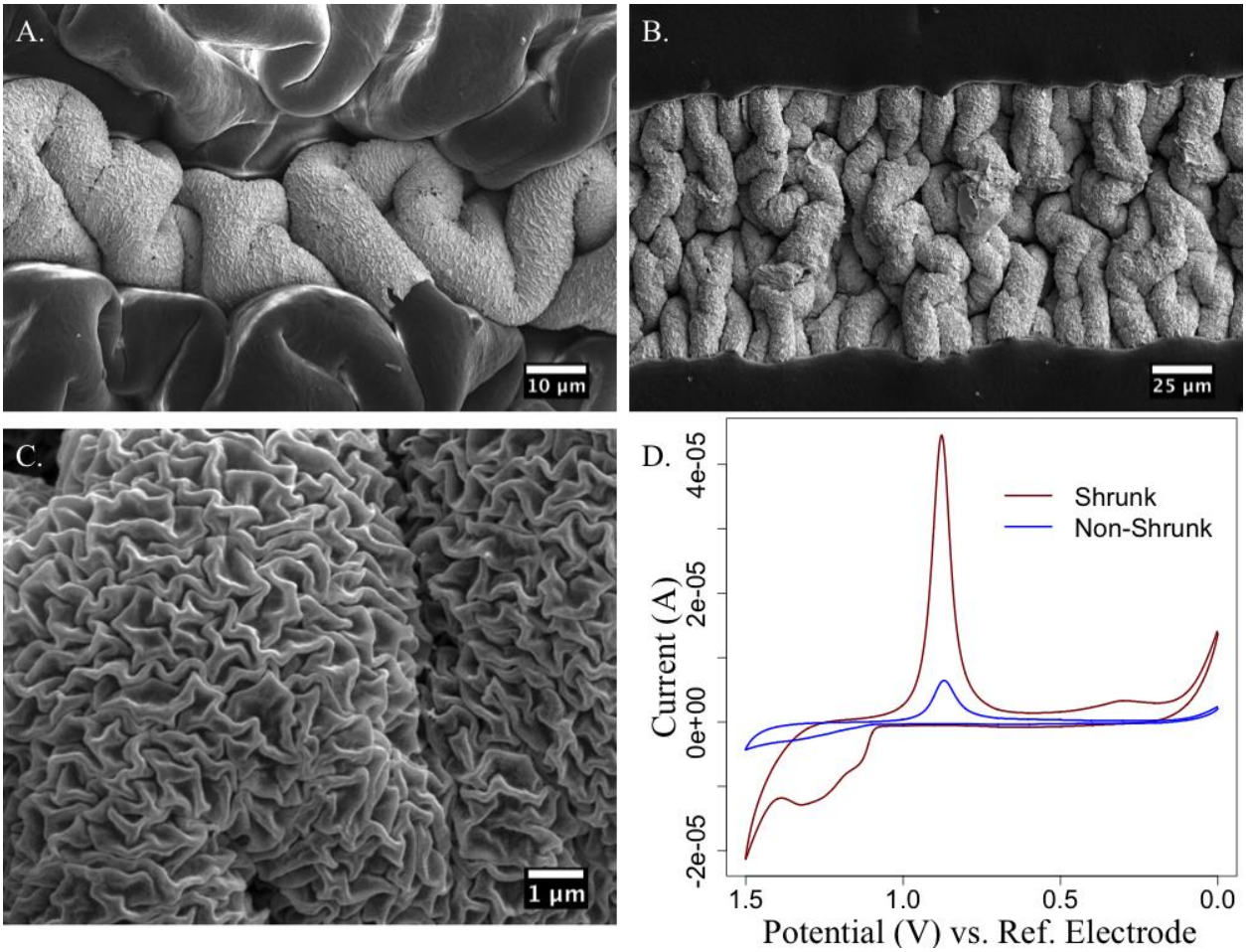

Figure 4 High surface area wrinkled thin film electrodes. A. with a rough, hydrophobic PO surface, B., with smooth PO surface, C. A higher magnification SEM shows the hierarchical electrode structure, D. Cyclic voltammetry shows >600% increased electrochemically active surface area over non-shrunk, planar electrodes.

films creates an increase in electrical contacts thereby circumventing these discontinuities and reducing the effective resistivity of the wrinkled thin film electrodes.

Cyclic voltammetry comparing exposed 2 mm x 2 mm areas of wrinkled verses flat Au thin film electrodes shows an improvement in electrochemically active surface area. Wrinkled Au thin film electrodes show a 647% enhancement as compared to flat thin films when integrating under the reduction peak of the CV diagrams (Figure 4B). This enhancement is lower than the theoretically calculated surface area given the amount the PO film shrinks. This is likely the consequence of a high-degree of aforementioned secondary folding. This result is consistent across

several wrinkled Au thin film devices suggesting reliable quality control between devices.

These hierarchical wrinkled structures (Figure 4A), aside from increased electrical performance, exhibit a high degree of roughness that leads to interesting interactions with liquid samples. It has been previously shown that heterogeneous, rough structures create anti-wetting behavior.[41,42] Additionally, creating large contrast between surface energies on a single substrate allows precise spatial control of small liquid volumes.[42] The contrast between patterned Au thin films and exposed PO areas allows for the same effect. Previously, it has been demonstrated that areas of contrasting surface energies yields very good spatial control and confinement of liquid droplets to specifically patterned regions.[42] Here, This same ability to confine liquid droplets to patterned Au detection zones on wrinkled PO surfaces is leveraged for parallel sensing of up to 15 individual samples in a device footprint of 1.5 cm x 1.5 cm (Figure 4).

5.3.2 Multiplexed ECL detection using digital camera

In addition to creating wrinkled Au thin film electrodes, subtle differences in the fabrication process can be used to modify the structure of the PO film surface surrounding the electrodes. Using the method outlined in Figure 2 results in a wrinkled PO surface as well as wrinkled thin film electrodes (Figure 5A). This is the due to plasma generation during ebeam deposition which oxidizes the surface of the PO film. This oxide thin film acts as a stiffness layer much like the deposited Au thin film.[44] This heterogeneous rough structuring increases the hydrophobicity of the polymer surface. The latter fabrication process described in the methods section leverages a photoresist lift-off process after Au deposition to protect the PO

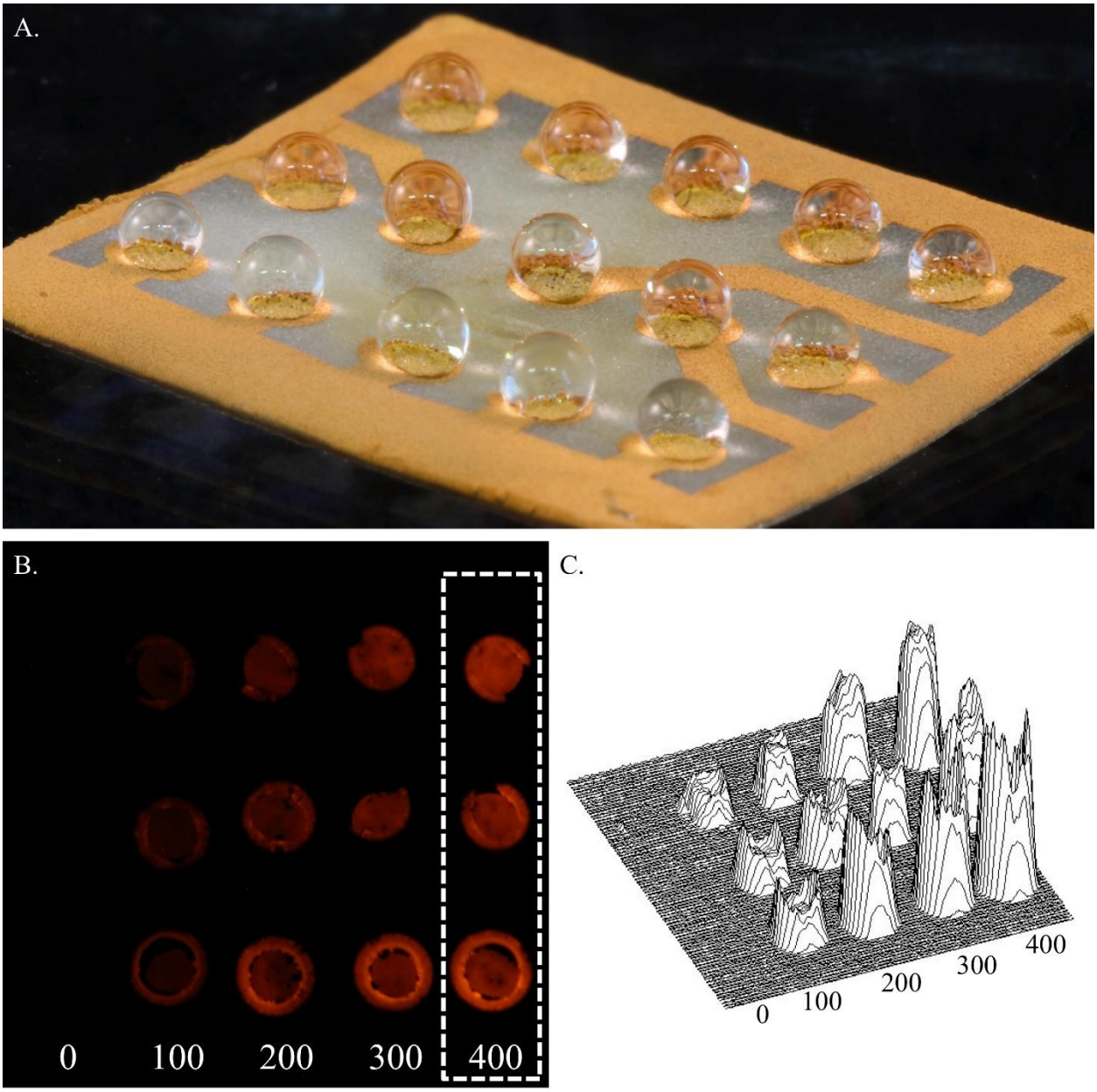

Figure 5 Shrunk ECL sensor. A. ECL sensor with wrinkled Au thin film electrodes spotted with 2 μL samples on patterned detection zones, B, Luminescent image from the CMOS sensor, C. A Surface intensity plot shows the detection zones where luminescent intensity is integrated for each DBAE concentration, Concentrations in μM.

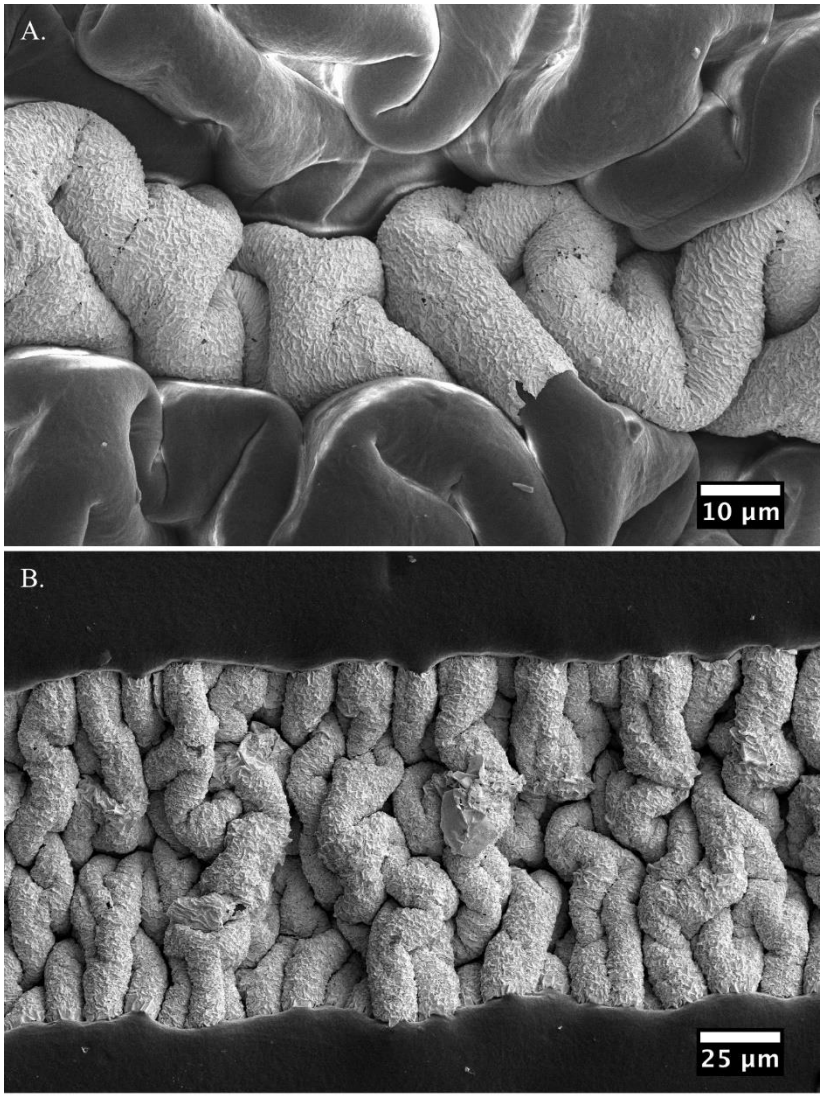

Figure 6 SEM of shrunk Au line traces. A. Wrinkled Au electrode along with wrinkled PO surface as a result of oxidation during ebeam deposition. B. Flat PO surface as a result of lift-off process.

surface against oxidation. When Au patterned PO films are shrunk using this approach, the bare polymer surface is flat and smooth (Figure 6B). This method provides the possibility for integration with microfluidics where a plastic top-sheet with microfluidic channels can be thermally bonded to the electrode layer.[75] In this demonstration, the first method was chosen for the ability to prevent any surface wetting of samples outside the patterned Au detection zones of our ECL sensor.

To show the utility and performance gains of these electrodes in a POC scenario, an integrated microdevice for ECL detection with an inexpensive digital camera was fabricated. Au patterned thin films on non-shrunk PO films served as a planar electrode control. Results for these Au wrinkled thin film electrode devices (Figure 5) showed detectable signals across the entire tested concentration range and a linear regime from 5 - 500μM and a LOD of 1.7 μM (Figure 7). This LOD is more than two orders of magnitude lower than similar paper-based ECL systems in literature[72] which also utilizes a consumer grade camera. The enhancement of electrochemical activity in the wrinkled electrodes is seen markedly at the higher end of the concentration range (Figure 7A). This is expected because the increased surface area of the wrinkled electrode increases the rate of electron transfer into the electrolytic solution for faster oxidation of the ECL complex. This translates to more luminescence when integrated over time by the CMOS camera sensor. The advantages of high surface area become less apparent at the lowest concentrations

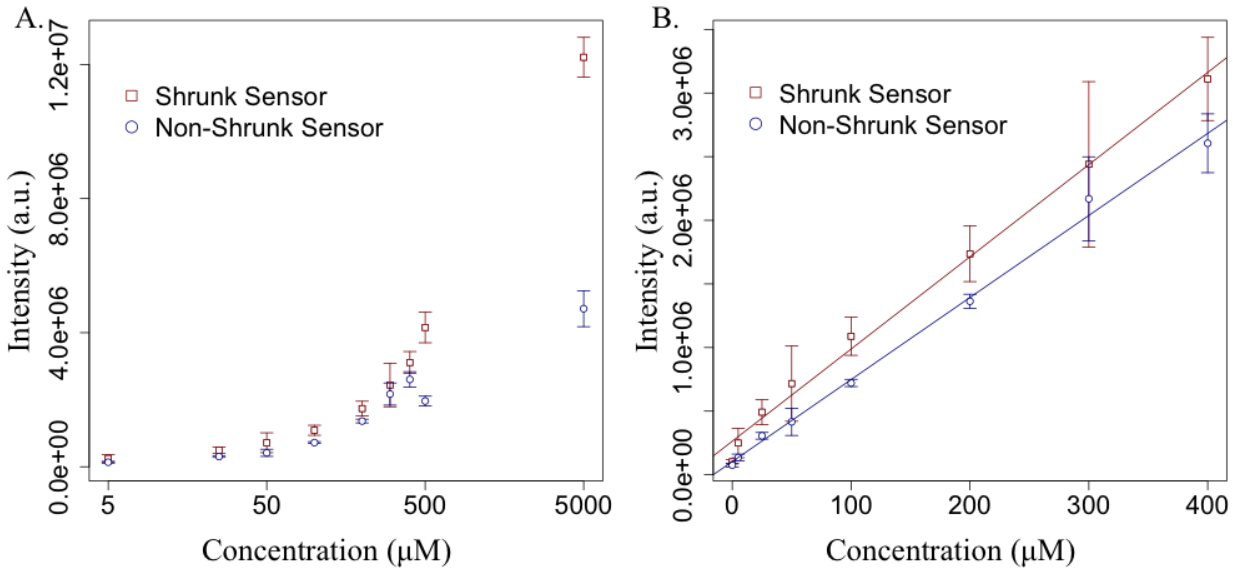

Figure 7 Concentration curves comparing planar and wrinkled electrode sensors. A. The full DBAE concentration range is shown on a log scale. B. The linear region of the concentration curve.

when the reaction rate is limited by the diffusion of DBAE to the electrode surface.

5.4 Conclusions

This chapter introduces an integrated plastic ECL sensor with shrink-induced high surface area electrodes using standard, scalable microfabrication techniques with commodity shrink-wrap film. Wrinkled Au thin film electrodes produced by thermally shrinking integrated shape-memory PO not only induces high surface area, but also, improves robustness and electrical properties. Integration of PO with standard micromachining processes provides reliable, higher resolution patterning as well as manufacturing scalability. Notably, with a 20-fold increase in resolution from shrinking, higher resolution can be achieved than with photolithography alone or any other previously reported methods using shape-memory polymers. In comparing planar and wrinkled thin film electrodes, wrinkled thin film electrodes show larger detectable signals, better range and sensitivity, and a LOD two magnitudes lower than similar existing systems.[72] These electrodes, integrated with a flexible thermoplastic substrate, are suitable for use with microfluidics or as conformal, wearable electrodes for microfluidic sweat sensing. These attributes make this technical innovation easily adapted for POC and mHealth applications.

6. Skin-Like Stretchable Strain Sensor

6.1 Introduction

Advances in mHealth monitoring has been stymied by a lack of available conformal sensors.[1–3] Wearable devices have seen some early success by packaging standard and/or flexible electronics to be adorned as “smart” fashion accessories for consumers. However, such sensor technology remains unable to produce accurate, quantitative biometric data to be usable for many mHealth applications.[1,4]

One of the most common sensors currently utilized is the tri-axial accelerometer. Many studies have focused on clever placement of these sensors and sophisticated algorithms to classify or analyze gait,[5] respiration,[6] and even fetal movement.[7] However, discernment of precision movement and extraction of signal from noise remains challenging with accelerometers alone. [1,8] For this reason, biometric data from an abundance of commercially available wearable devices are often reduced to less specific quantitative measurements such as "activity."[1,8,9]

Strain sensors are a promising addition to accelerometers for wearable applications. Strain can be used to determine pressure,[83–85] displacement,[54,86] bending angle,[17,87] and acoustic vibrations.[12,85] These metrics can be combined to establish quantitative measures for monitoring human movement as it relates to athletic performance,[27] rehabilitation,[88] or physical symptoms from drugs or illnesses.[1] With this goal in mind the rapidly maturing field of flexible electronics has made tremendous strides towards developing new, mechanically compliant transducers in order to enable wearable devices to unobtrusively acquire biometric signals.[89–92] As such, wearable strain sensor development has seen research focused towards stretchable capacitive, percolating, and piezoresistive (PR) sensor types.

Capacitive sensors utilize compression of the dielectric layer, which is caused by either normal pressure or Poisson ratio changes from in-plane strains. These types of sensors can exhibit excellent sensitivity for detecting subtle movements such as pulsatile pressure.[84,93] Li *et al.* developed a wearable pressure sensor on flexible PET film with transparent ITO electrodes and ionic gel dielectric. By integrating into a low profile cuff, they show the potential for effective monitoring of chronic venous disease using capacitive pressure sensors.[84] However, with parallel ITO electrodes on PET films this device is flexible but not stretchable to cope large strains. Larger strains such as those required to measure gross body movements are also attainable using

capacitive strain sensing. Zens *et al.* demonstrates this using interdigitated electrodes on elastic silicone to quantify knee laxation for post-operative rehabilitation monitoring.[87] Although the dynamic range for strain is often sufficient for the intended application, these sensors can suffer from poor sensitivity, gauge factors (GF) <1, or capacitive interactions with the body which limit direct epidermal application.[17]

Percolation strain sensors are often thin composite materials containing conductive networks of micro/nano particles. When stretched or compressed, the relative density and/or degree of contact of these conductive networks change, reflected in change in resistance. Percolating sensors can also be optimized for either small or large strains. Gong *et al.* demonstrated pulse detection by placing a percolating network of gold nanowires over an interdigitated electrode pattern on a PDMS substrate.[85] Pan et al. has shown through rationally designed conductive polypyrrole (PPy) hydrogels[94,95], high sensitivity at ultra-low pressures (<1Pa) and a medium pressure saturation threshold (~100 kPa) is possible.[96] Importantly, the use of the hydrogel reduces viscoelastic effects when compared to other elastic polymers, however, rapid aging of the PPy in air causes electronic drift and thus relies on effective device packaging. Dense networks of carbon nanotubes (CNT) can be used to measure larger strains in part due to their high electrical conductivity and robust mechanical properties. Amjadi et al. demonstrate the ability to measure joint flexion with such CNT devices, which can record strains in excess of 60%.[17] Although many of these sensors show good linear response with low hysteresis over very large strains (>1000%),[21] it is often at the expense of sensitivity (GF < 1).[17,21,23] Moreover, sensitivity in percolating type sensors can be very high, but at the tradeoff of a limited dynamic range; this necessitates more complex architectures to achieve both high GF and a large dynamic range.[54,96]

Wearable PR sensors often employ thin conductive materials that exhibit resistance-strain dependence primarily from geometric changes and controlled fracturing or crack propagation in the sensing film upon applied strain.[83] This leads to a tremendous amount of tunability in both sensitivity and dynamic range with lithographically defined geometries[11,97] and materials choices.[11,12,22,86,98,99] Very high sensitivity can be achieved, as demonstrated by Kang *et al.*, by utilizing relatively brittle platinum (Pt) thin films to detect sound vibrations for word recognition with a GF > 2000 and a dynamic range of 2% strain.[12] Recently, Yong *et al.* produced wrinkled graphene PR strain gauges with a modest GF of ~2.8 and dynamic range of 100% strain.[100] Large dynamic range (>100%) is possible using alternate materials, however, often yielding low strain sensitivity.[13,101,102]

Here hierarchical wrinkled structures into Pt thin films (wPt) which perform as PR strain sensors is introduced. These micro-nanowrinkles in the wPt thin film, supported on skin-like silicone rubber, enhance the dynamic range (>100% strain) while also attaining good sensitivity that is inherent to Pt thin films (GF = 42 at 185% strain). The highest GF was reported under semistatic linear strain conditions as is commonly reported.[18,24,86] To my knowledge this represents the highest GF over a large, and physiologically relevant, range of any metal thin film strain sensor for on-the-skin applications.[11,16,101,103] Tunable sensitivity and dynamic range is achieved by changing wPt film thickness. Tthe potential of this sensor in mHealth monitoring by indirectly quantifying lung volume correlated to chest wall displacement during respiration is demonstrated. Further, this wPt sensor can be lithographically defined using standard semiconductor equipment and materials. Therefore, these sensors can be optimized for many wearable applications and scaled to production with roll-to-roll processing.[45]

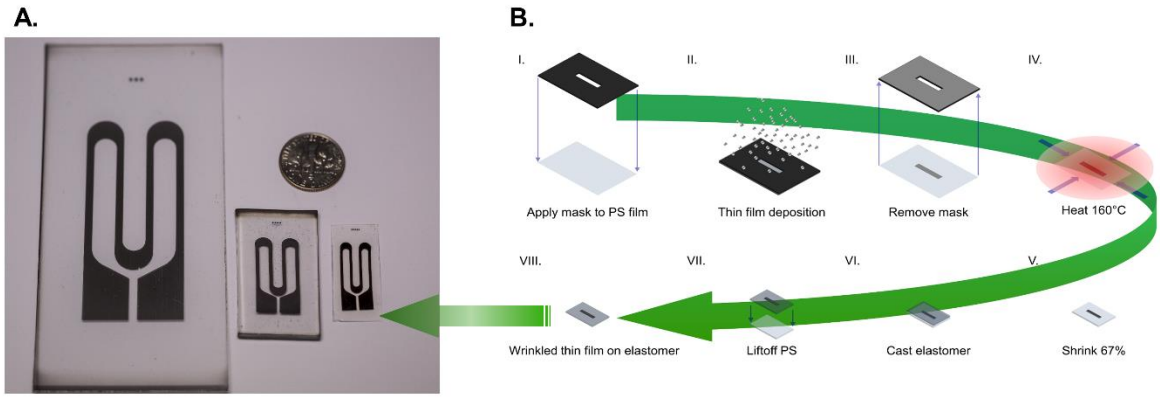

Figure 8 shows (A, left to right) as deposited, wrinkled, and transferred wPt strain sensors with a US dime for scale and (B) an illustration of the fabrication process flow.

6.2 Experimental design

6.2.1 Fabrication of wPt strain sensors

Sensor designs are drawn using computer aided design software (Autodesk). The sensor design is laser machined (Versa Laser, VLS2.30) into a single-sided adhesive polymer film (Grafix Arts, Frisket Film) to create a mask. This mask is adhered to a pre-stressed polystyrene (PS) film (Grafix Arts, KFS50-C). A 5 nm Pt thin film is deposited onto the masked PS film using a timed magnetron sputter deposition (Quorum Technologies, Q150R) of 207 s. For 25 nm and 50 nm thick Pt films, samples are sputtered for 1057 s and 2124 s, respectively. A second layer of 5 nm Au is sputter deposited (102 s) onto the Pt thin film. The mask is then lifted off the PS film, leaving the desired metal thin film sensor design (Figure 8). The sample is subsequently placed into a convection oven at 160°C for 5 minutes to induce the thermal miniaturization process. The sensor design is shrunk to 33% of its original size, creating wrinkles in the metal thin film, which, as previously shown, reduces resistivity[42]. An adhesion promotor is used to reliably transfer the wPt and Au thin film to EF30 (Smooth-on, Ecoflex 0030). The shrunken sample is placed in a 5mM (3-Mercaptopropyl) trimethoxysilane (Sigma Aldrich, 95% MPTMS) in ethanol bath for 1 hr

before air drying. EF30 is poured immediately onto the MPTMS treated samples and spin coated at 150 rpm for 35 s. Following spin coating, samples are placed under vacuum for 20 min and then removed to cure at 85 °C for 2 hrs. The wPt thin film is then transferred onto EF30 by lifting off the PS layer in an acetone bath for 30 min at 75 °C. Once the PS layer has lifted off, the samples are dipped in a toluene bath and immediately washed with acetone. This final wash process is repeated as necessary to ensure removal of all residual PS from the wPt thin film. Finally, the strain sensors are left dry in a fume hood for 1 hr.

6.2.2 Sheet resistance

Measurements were taken with a four-point probe station combined with a rapid source measuring unit (Keithley, 2612B Source Meter). The voltage was set to 100 mV, and the resulting current was measured. The Van der Pauw method was then used to determine the sheet resistance value. Separate samples were prepared with 3 nm of Ir for visualization using SEM (FEI, Magellan).

6.2.3 Strain characterization

Strain sensitivity of wPt sensors was determined using a semi-static tensile strain testing apparatus. Resistance is recorded at 5% strain increments until failure. Additionally, sensors pre-conditioned at 100% strain were subjected to subsequent cyclic fatigue testing by straining sensors from 0% to 50% using a saw-tooth waveform on a computer controlled linear strain testing apparatus. The samples were cycled 1000 times at 4mm/s.

Response time was measured by rapidly (13.6 mm/s) tensioning the sensor to 50% strain and holding for 10 s. The sample was then released at the same rate back to 0% strain and held for 10 s before beginning the next cycle. Response and relaxation time is reported from the tenth cycle.

6.2.4 FEA modeling conditions

A simplified 2D finite element analysis (FEA) was performed using Ansys workbench 16.0. A cross sectional geometry was created with hierarchal wrinkle structures; the model consists of two metallic thin film of Au and Pt on top of an EF30 substrate. The Au and Pt were modeled as isotropic elastic material with Young's modulus of 69.1 GPa and 139.7 GPa, respectively.[104] The EF30 was modeled with a two parameter Mooney-Rivlin hyperelastic model.[105] The finite element analysis was performed with 50 and 100 percent strain.

6.2.5 FFT parameters

To find the wavelength distribution of the wrinkles, a 2D Fast Fourier Transform (2D FFT) was applied to a sectioned top down SEM image of the sensor surface. The absolute value of the 2D FFT output was readjusted such that the zero wavenumber, defined as 1/wavelength, started at the center and the largest wavelength ended on the edge. The intensity values were then summed radially for each wavenumber to create an intensity versus wavelength profile. Afterwards, the intensity was adjusted for noise by subtracting the total background noise at each summation, and the profile was normalized to the largest intensity value. Lastly, only the relevant range of wrinkle wavelength was graphed as intensity versus wavenumber.

6.2.6 Chest wall displacement sensor setup

Finished wPt sensors were attached to athletic tape (KT Tape, cotton sports tape) and applied across the subject's external intercostal muscles. Lung volume dynamics were measured using a digital spirometer (Contec, SP10) and were correlated to characteristic chest displacement signals as measured by the wPt sensor. Resistance changes in the sensors undergoing strain during respiration were converted to voltages using a type-1, quarter-bridge configuration Wheatstone circuit and a low-gain differential amplifier. These voltages were acquired at 40 Hz by a small 10-

bit microcontroller (Atmel Corp., ATmega328) and then transmitted via Bluetooth 4.0 to a real-time monitoring application.

6.3 Results and discussion

6.3.1 'Shrink' fabrication and transfer

Stiff thin film materials buckle and form complex hierarchical wrinkles in response to compressive stress of shape-memory polymer (SMP) carrier films.[36] These wrinkled structures have proven useful for increasing sensitivity and/or efficiency of electrochemical,[49] optical scattering,[50] SERS,[106,107] and various other sensors.[43,51,108] Often, wrinkled thin film structures robustly integrate with the SMP carrier films using the aforementioned processing techniques, limiting the final device material to a rigid or flexible thermoplastic. Transferring the wrinkled thin film onto other materials allows for the same enhancements provided by the hierarchical wrinkled thin films to apply towards applications unsuitable for non-stretchable SMPs. This is especially the case with wearable sensors and mHealth, where a device is conformable to curvilinear surfaces and mechanically similar to human skin. The method demonstrated in this work builds on previous shrink fabrication methods by introducing a SMP lift-off and transfer of PR wPt thin films onto biocompatible EF30 elastomeric silicone (Figure 8). This silicone supported wPt serves as a skin-mountable strain sensor with potential for use as a wearable mHealth monitor.

Table 1 sheet resistance of bimetallic thin film. (V=100 mV)

Pt:Au Thickness (nm)	As Deposited (Ω/sq.)	Wrinkled (Ω/sq.)	Transferred (Ω/sq.)
5:5	3068 ± 274	724 ± 97	1243 ± 15
25:5	3954 ± 363	501 ± 30	1070 ± 214
50:5	2711 ± 438	419 ± 91	1031 ± 160

The Pt thin film is sputter deposited through a physical mask onto a polystyrene (PS) SMP support film similar to previously reported works.[13,49] Three Pt film thicknesses where tested: 5, 25, and 50 nm. A 5 nm thin film of Au is then deposited in order to strongly adhere the thin film to EF30 using (3-Mercaptopropyl) trimethoxysilane (MPTMS) chemistry[10] upon transfer. Prior to MPTMS treatment the patterned thin film on SMP is thermally shrunken by 67% in area to create the wPt thin film. Then MPTMS is linked to the Au film and uncured EF30 is molded on top. Once the EF30 has cured, the PS support is lifted-off using organic solvents. This leaves the wPt thin film, now supported on skin-like EF30 (Figure 8B).

6.3.2 Tunable strain sensors

Sheet resistance was compared between as deposited, wrinkled, and transferred thin films (Table 6.1). Sheet resistance decreases substantially upon thermal shrinking of the as deposited thin films. This effect has been previously studied, in brief bi-axial compression of thin films bridges discontinuities in as deposited thin films whereby lowering electrical resistivity.[47,49] Sheet resistance increases between wrinkled and transferred thin films. However, transferred thin film sheet resistances remain ~65% lower than those of their as deposited precursors. Sheet resistance for 5, 25, and 50 nm wPt thin films are 1243, 1070, 1031 Ω/□ respectively. This suggests that the transfer process maintains good integrity of the wPt. Moreover, during fabrication of the wPt strain sensors, an Au thin film and MPTMS treatment is used to irreversibly adhere the piezoresistive Pt thin film to EF30. Therefore, sheet resistance measurements reflect the Pt and Au bimetallic layer. Importantly, sheet resistance measured before the wPt is transferred onto silicone have probes contacting the Au surface whereas probes contact the wPt when measuring sheet resistance after

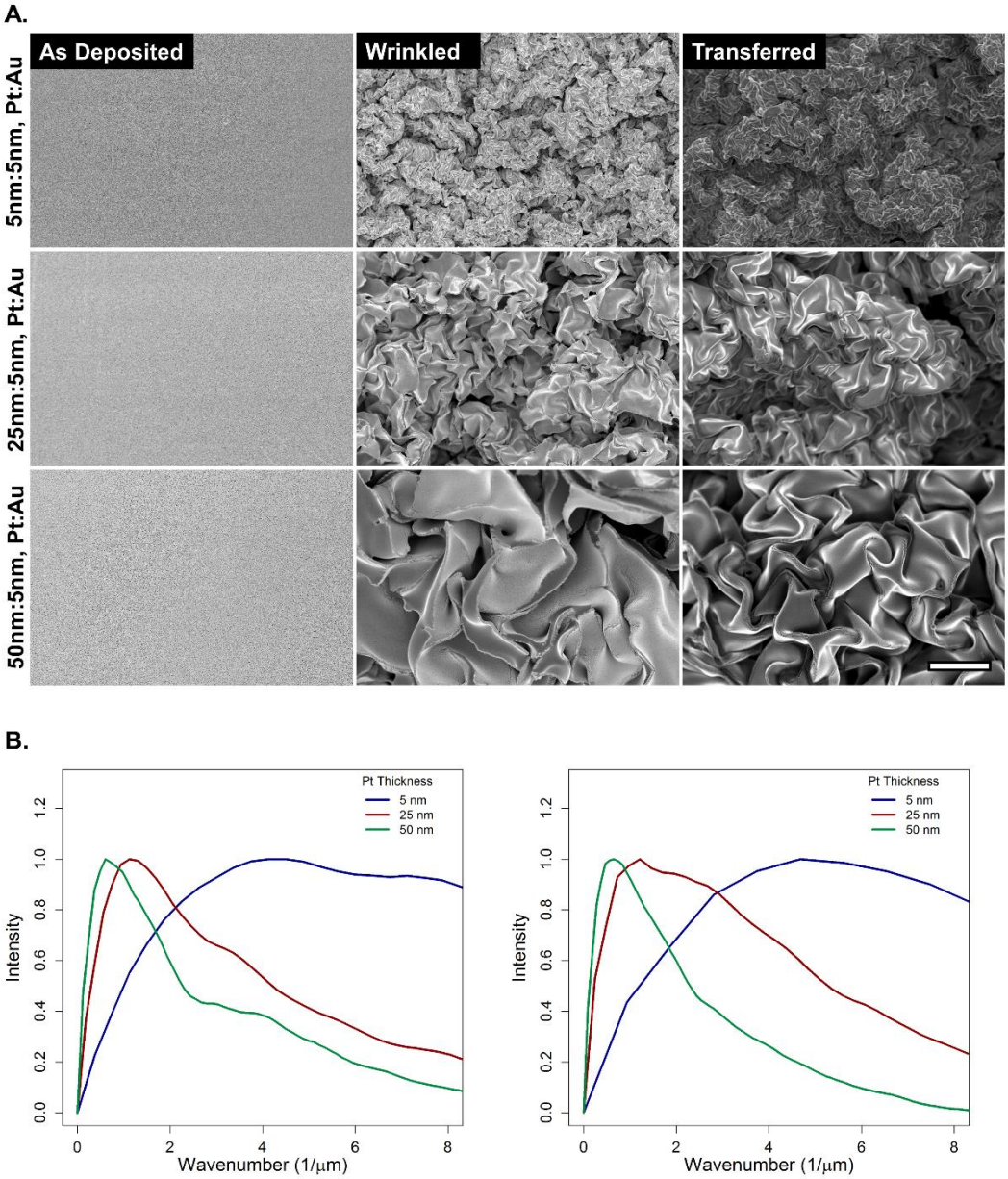

Figure 9 shows (A) SEM of as deposited, wrinkled, and transferred Pt thin films at 5, 25, and 50 nm. All micrographs are at equivalent magnification. Scale bar is 5 µm. (B) shows FFT performed on wrinkled (left) and transferred (right) SEM showing the frequency of different length scale features.

the transfer. Indeed, visualization under SEM further suggests good integrity of the wPt thin film to also preserve the complex hierarchical structure (Figure 9A) after transfer.

Feature size of the wPt increases with film thickness (Figure 9B). This results in a decreased density of wrinkling and increased fracturing of the brittle Pt thin film prior to transfer as film thickness increases. I theorize that the density of the wrinkles plays a vital role in the controlled fracture of the wPt sensor, affecting both dynamic range and GF as will be discussed in the following section. The dynamic range of wPt strain sensor can be tuned according to film thickness as shown in semi-static linear strain tests with 5, 25, and 50 nm thin film sensors (Figure 10A). Multiple sensors of each film were tested (Figure 11) and the best performing are represented in Figure 10A.

Thinner wPt thin films demonstrate the highest dynamic range with maximum strains as high as 185%. I theorize this is due to a combination of both more malleable mechanical properties of the 5 nm Au thin film and a higher density of wrinkles. As the Pt film thickness increases, the mechanical behavior is ever dominated by the comparatively brittle wPt. This results in more fractures prior to strain and most importantly a lower density of nano/microwrinkles in the thicker 25 and 50 nm wPt films. Lower density in wrinkles results in less stress relief in the wPt thin film as will be discussed in greater detail in the following section. Strain sensitivity therefore increases in these thicker samples yielding higher GF at lower strains when compared to thin films with higher wrinkle densities. At equivalent strain, 50 nm thick wPt displays the highest GF of 27 at 95% strain whereas 25 nm and 5 nm thin films show lower GF of 20 and 9, respectively. However, the 5 nm wPt sensor achieves the absolute highest GF of 42 at 185% strain.

Durability of 5 nm wPt samples was also studied, applying multiple tensile cycles to 50% strain at 4 mm/s (Figure 10B) for 1000 cycles. These samples were first conditioned by being

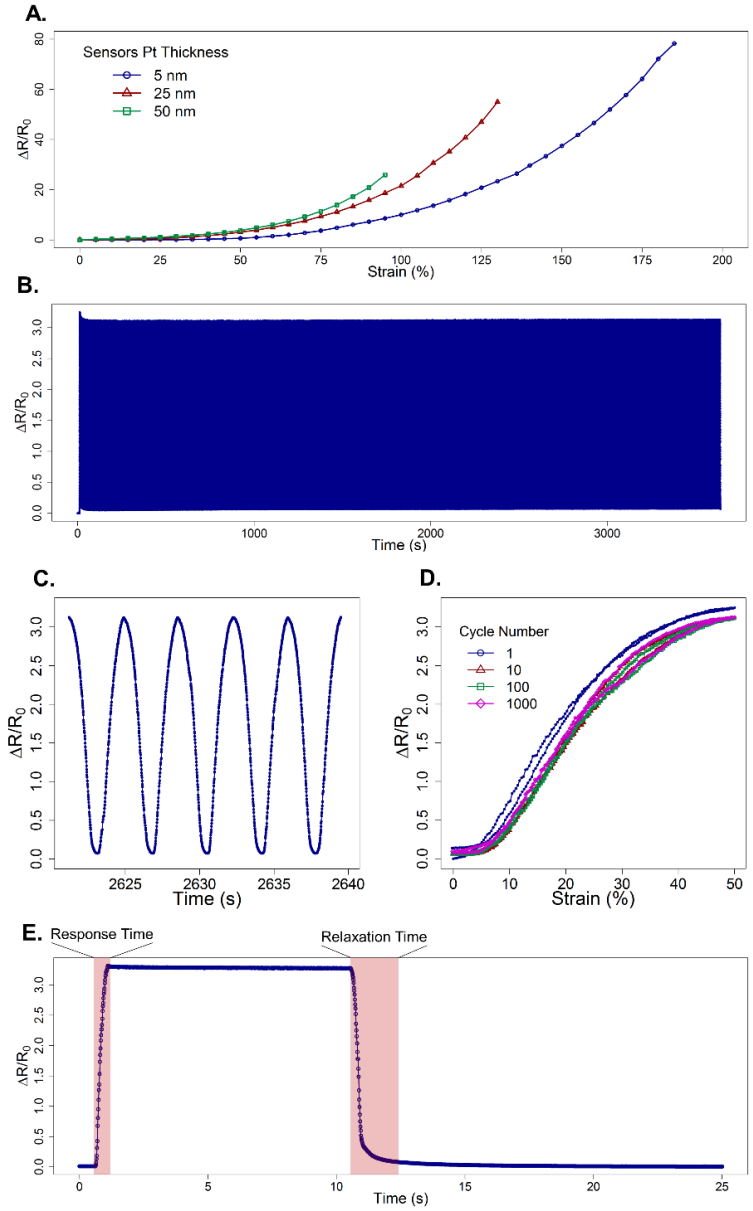

Figure 10 shows (A) the strain sensitivity of the best performing 5, 25, and 50 nm wPt strain sensors. (B) 5 nm wPt sensors underwent 1000 cycles of a tensile strain for durability testing. The samples were preconditioned at 100% strain, then subsequently cycled continuously at 50% strain at 4 mm/s. (C) shows a small subset of strain cycling to show the repeatability and stability of the sensor. (D) plots select tensile and relaxation cycles of percent resistance change vs. strain which shows a very brief conditioning phase followed by consistent performance with low amounts of hysteresis. (E) Shows a sensor rapidly strained to 50% and held for 10 s before rapidly returning to 0% strain in order to quantify response and relaxation time. Due to viscoelastic properties present in the processed EF30 polymer relaxation time are elongated as compared to the speedy response time.

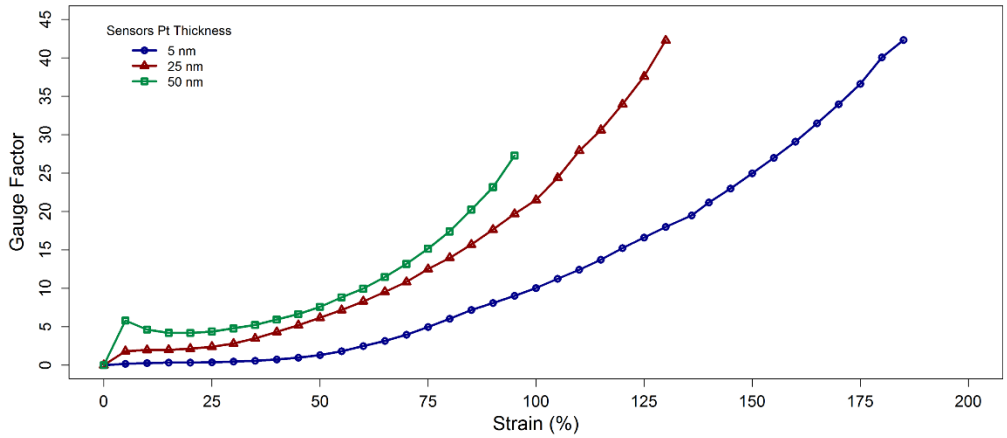

C.

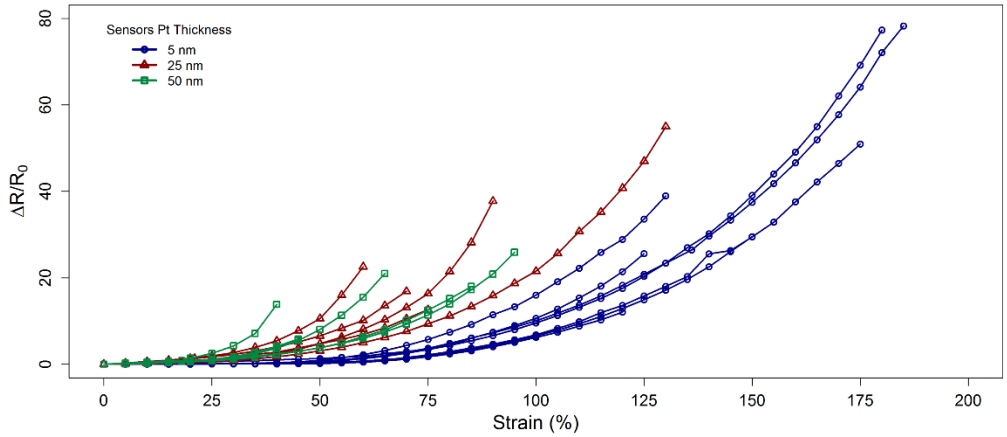

Figure 11 shows the gauge factors versus strain of the samples shown in Figure 10. At equivalent strain the 50 nm wPt sensor shows the highest sensitivity to strain, however, the 5 nm wPt sensor has the highest gauge factor at a maximum strain of 185%. (C.) shows all of the sensors tested in order to establish strain sensitivity according to thin film thickness.

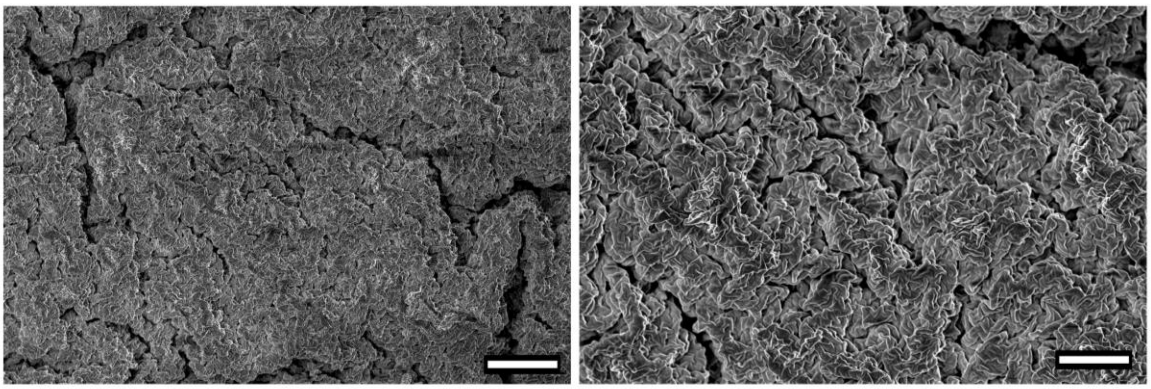

Figure 12 shows SEM of the 5 nm thick wPt after 6500 strain cycles demonstrating integrity of the thin film is maintained with no apparent delamination from the EF30 elastomer support film. Scale bar is (left) 10 µm and (right) 5 µm.

stretching out to 100% strain (data not shown) before beginning cycled continuously at 50%. During repeated straining the sensor still shows a brief conditioning phase in the first few cycles. However, when the sensor becomes conditioned after multiple cycles, hysteresis is significantly reduced and the sensor performance is stable through the end of the test. The sensor displays excellent reproducibility with little to no change in hysteresis between cycle 10, 100 and 1000 (Figure 10D). Important to note that unlike the semi-static linear strain testing (Figure 10A), sensor response to strain cycling (Figure 10D) is rate dependent. Sensors where cycled as many as 6500 times without failure or apparent delamination of the wPt from the EF30 support film (Figure 10).

Sensor response time of 0.5 s shows no latency from the time required to actuate the sensor on the test fixture and the sensor reading within 10% of the sensor saturation value (Figure 10E). Increasing the response time criteria to within 1% of saturation increases response time to 0.6 s representing a latency of 0.1 s. However, relaxation time suffers from the viscoelastic effects of the processed EF30. Because organic solvents were used during the lift off process, the EF30 appears to suffer from rapid aging where by increasing the viscoelastic effect upon relaxation from tensile straining. Therefore, relaxation time is elongated to 1.3 s to reach a value within 10% of

baseline value, representing a latency of 0.8 s. However, stricter criteria to reach within 1% of baseline resistance increase response time dramatically to 7.6 s, a 7.1 s latency. This also accounts for some of the hysteresis seen when performing repeated tensile cycle testing. Better response times and lower hysteresis can be achieved by transferring wPt thin films onto polymers with higher chemical resistance to organic solvents and / or shorter elastic response times.

6.3.3 Mechanism for tunable stretch sensitivity

I theorize that the PR response to strain of the wPt thin films contains multiple phases, which result in the non-linear strain sensitivity. There are three primary phases: in-plane elongation, fracture nucleation, and fracture elongation. Resistance changes during in-plane elongation is primarily due to separation of adjacent wrinkle structures and lengthening of the geometry. Strain sensitivity increases with the fracture nucleation phase at moderate to high strain, and sensitivity increases rapidly as those fractures begin to elongate near maximum strain. A finite element model (FEM) of a hierarchical bimetallic thin film with simplified geometry was used to better understand the controlled fracturing of the wPt sensor (Figure 13). Concentration of stress is similar to results previously reported by other groups employing 2D fractal serpentine structures.[97,102] As the model suggests, stress is concentrated at the high angle bend, or valleys of the thin film. This is where micro-cracking nucleates at high strains (Figure 13). Therefore, with increased density of wrinkles in the thin film, the nucleation phase for fracturing is distributed over a longer range of strain as each new fracture point relieves stress in the thin film. Therefore, increase wrinkle densities provides more strain relief in wPt thin films, increasing the strain sensor range. These multiple points of fracturing also forms a mesh-like structure in the thin film. As strain increases, the fracture nucleation points in the wrinkle valleys are exhausted. These fractures

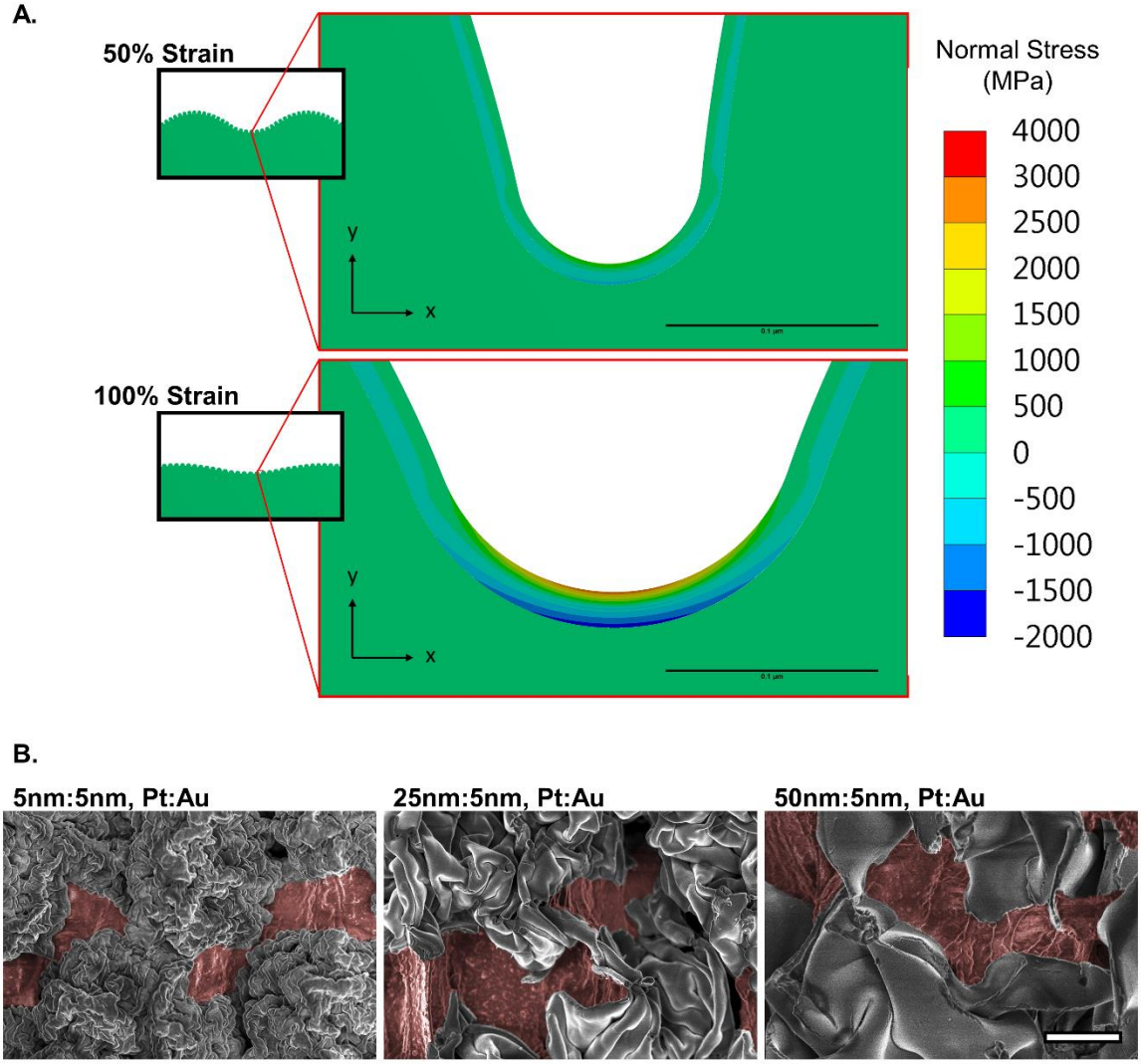

Figure 13 (A) shows a FEA model showing stress in the wPt and Au bimetalic thin film when fixed on top of an elastomeric substrate at 50% and 100% strain. Strain was applied along the x-axis. The model shows that upon strain, stress is concentrated in the valleys of the serpentine wrinkled structure. (B) shows SEM of wPt thin films at 100% strain. Fractures in the thin film have been made more visible by pseudo-coloring the exposed polymer support layer red. All SEM are at equivalent magnification and the scale bar represents 5 µm.

then begin to elongate, coalescing with adjacent fractures in the thin film mesh until the thin film ruptures completely. This behavior is similar to other mesh patterned Au thin film.[11] Thicker thin films have a lower density of fracture nucleation sites as a result of the larger wrinkled pattern. The elongation phase, therefore, begins at lower strains and results in higher strain sensitivity.

It is important to note that this order of events for fracturing thin films is only possible through strong adhesion between the thin film and the elastic support material. Research has shown that polymer material plays an important role in evenly distributing stress throughout a thin film.[14–16,109] Therefore, the Au and MPTMS adhesion layer is important for repeatable fracturing behavior. Without an adhesion layer, wPt delaminates from EF30 under minimal strain. This concentrates stress in that delamination area and causes premature failure.[16,103] Unlike previous works that demonstrate the importance of strong adhesion to polymer substrate with Au films,[11,13–15,109] the use of wPt, which is relatively brittle by comparison, in this work exhibits increased sensitivity to strain.

6.3.4 Monitoring respiration

A 5 nm wPt sensor was placed onto the left external intercostal muscles of the chest wall (Figure 14) with adhesive tape to measure chest wall displacement during respiration. This region was selected because of its characteristic displacement during the breathing cycle caused by the contraction and relaxation of underlying inspiratory muscles.[110–112] A spirometer was used in conjunction with the wPt sensor in order to correlate inspiration capacity (IC) and tidal volume (TV) with sensor displacement (Figure 14D). The spirometric measurements showed the subject was able to expel 95% of his IC, calculated by the digital spirometer based on the subject's physical build (height and weight). The subject followed this maximal exhale with normal tidal breathing. The wPt sensor's strain amplitudes corresponding to the spirometric tests were correlated with the

measured IC volume, producing a lung volume metric approximated by chest wall displacement. Strain sensor measurements show that the subject's TV (small peaks following the maximal peak) is approximately 600 mL and the IRC is 3500 mL, both well within the subject's expected physiological range. Evidence of hysteresis in the sensor is apparent however, since strain amplitudes are slow in returning to baseline readings. Adjustments can be made in future designs to reduce offset by utilizing a more responsive polymer support for the wPt thin film.

6.4 Conclusion

A wPt thin film sensor capable of measuring strain as high as 185% with a high GF of 42 is presented in this work. To my knowledge, this represents the highest sensitivity of any metal PR strain sensor with a dynamic range suitable for almost any skin-mounted application. A table comparing the presented sensor with similar technologies is presented in Table 2. Importantly, these wPt sensors can be tuned for different dynamic ranges and sensitivities as required by the application. Furthermore, the potential of such a wearable sensor for mHealth applications by indirectly measuring lung volumes during respiration. Development of classification algorithms for distinguishing between various physical states (i.e. exercise and rest) based on sensor readings will also be incorporated in future efforts to automate analysis of human respiration.

Table 2 Sensitivity and dynamic range of current wearable strain sensors

	Thin Film Material	**Gauge Factor**	**Dynamic Range**	**REF**
Pegan *et al.(this work)*	Platinum	42	185%	[113]
Kang *et al.*	Platinum	>2000	2%	[12]
Bae *et al.*	Graphene	14	7.1%	[114]
Lee *et al.*	Silver	2	20%	[115]
Zhu *et al.*	Gold	1	100% (135% max)	[116]
Kim *et al.*	Gold	0.07	70% (200% max)	[13]
Commercial Sensors	Metal Foil	2-5	~5%	[117]

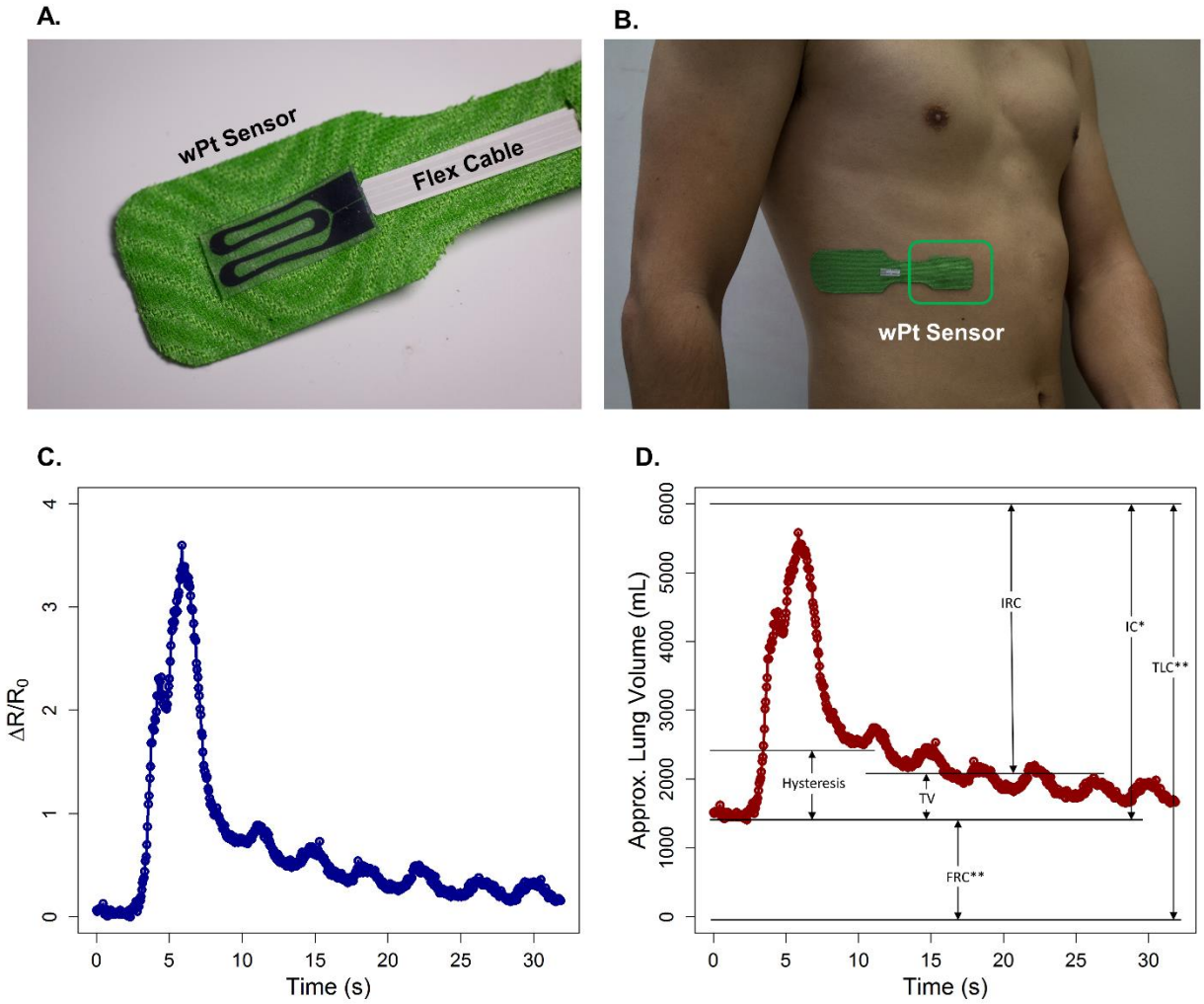

Figure 14 shows (A.) shows (A.) a wPt strain sensor contacting a conductive flex cable and placed on stretchable athletic tape. This sensor was place on (B.) the intercostal muscles in order to measure chest wall displacement during respiration. The sensor was connected via the flex cable to a prototype board (not shown) with Bluetooth connectivity in order to transmit and log data on a computer. (C.) shows the signal from the sensor resulting from chest wall displacement during respiration. Using spirometer readings, (D.) approximate lung volumes where correlated to sensor data. *spirometer reading show inhale and exhale as reaching 95% of IC. **volumes calculated based on subject's physical parameters.

7. Future Directions

7.1 Transfer carrier materials and processing

7.1.1 Rapid polymer aging

As is evident in chapter 6, the wearable sensor suffers from some viscoelastic dampening during relaxation of the sensor when used to monitor breathing. This is likely exacerbated further by covering the sensor with adhesive tape. Preliminary mechanical testing of EF30, both virgin and solvent treated (similarly to the lift off protocol in chapter 6), reveals that the polymer is negatively affected by the solvent treatment (Figure 15). Results show that the modulus increases as well as the relaxation time. Table 3 shows the modulus measured EF30 modulus determined from mechanical testing. It is likely that the solvent is rapidly aging the EF30 and increasing the apparent viscoelastic behavior and stiffness.

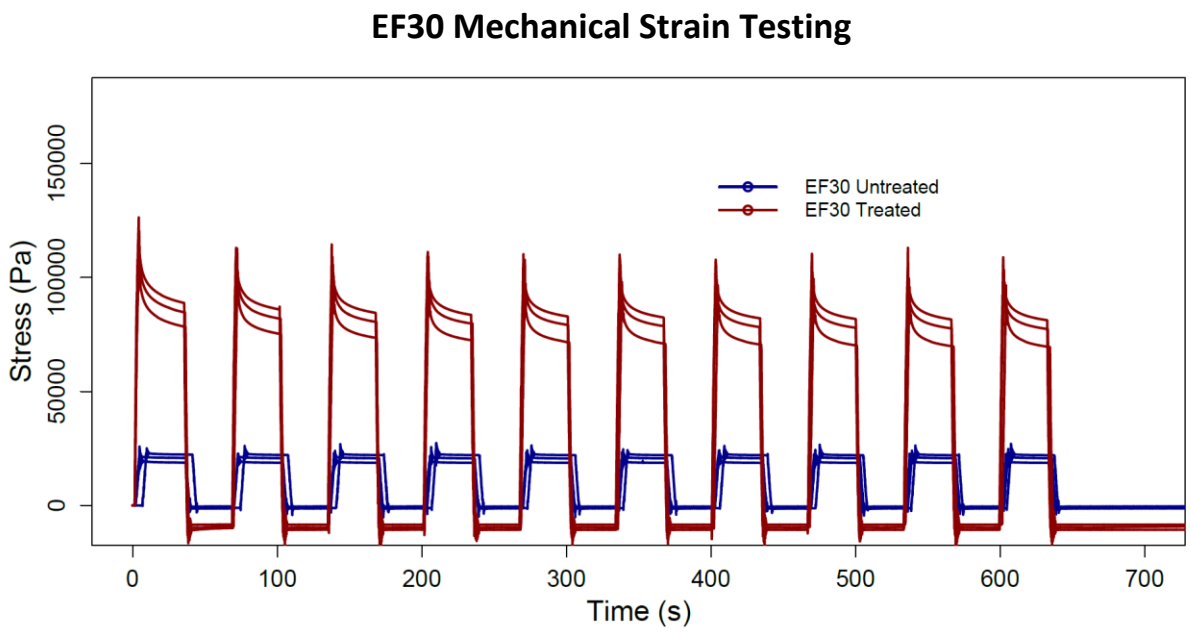

Figure 15 shows stress cycling of virgin and solvent treated EF30. Applied strain is 100%.

Table 3 displaying EF30 factory specification and effective modulus at 100% strain

	Modulus
EF30, Virgin	*24 kPa*
EF30, Solvent Treated	*106 kPa*

7.1.2 Water soluble sacrificial layer

One possible solution to EF30 susceptibility to organic solvents is to remove acetone and toluene from the transfer process. Instead a water soluble sacrificial layer, such as a hydrophilic polymer[118] can be incorporated under the wPt film. Then the wPt layer can be lifted off without aging the EF30 polymer. While there are many candidate polymers, Polyacrylic Acid (PAA) is an attractive candidate due to its reversible crosslinking (and thereby degree of solubility) with a simple ion exchange.[118]

However, inserting a sacrificial layer into the process will likely affect each step in the process following the deposition of a PAA film. Specifically with regards to metal-polymer adhesion and temperature restrictions. Dissolving PAA in water is a slow process,[118] and the added wrinkled caused by shrinking could dramatically increase the lift off time. Importantly, this film could also alter the performance of the device as PAA film thickness ranges on the order of 100 – 300 nm, two magnitudes thicker than the deposited thin film in chapter 6. Conversely, the addition of a sacrificial layer would allow for tuning the size of the wrinkles of the metal without having to change the deposited metal thickness.

7.1.3 Chemically resistant polymers

Another solution besides removing organic solvents from the transfer process would be to select an elastic silicone with better chemical resistance. There is a large variety of medical grade

silicones which would effectively replace EF30. After considering chemical resistance, the mechanics of the polymer must match the on-skin application. Polymers with less apparent viscoelastic behavior would benefit the responsiveness of the sensor. However, these materials tend to be much stiffer with much higher moduli. A high modulus can be overcome by thinning the physical thickness of the silicone carrier much to the same effect as metal thin films are appropriate for on-skin applications despite a modulus in the Gpa range.

7.2 Correlating sensor data with health parameters

Finally, the ultimate success of remote health monitoring and other mHealth applications will be the adoption of this type of wearable technology by users/patients and physicians. For this to become a reality, data collected from wearable sensor must be connected/correlated to impactful physiological health parameters. For applications in breath monitoring this could mean correlating breath rate and lung volume with a patient's peak oxygen consumption (VO_2max). This work can be done by using the presented wearable strain sensor to measure against spirometry. With the aid of sophisticated computer classification algorithms and other machine learning tools, correlations and predictive models can be established to give wearable sensor data physiological impact. This future direction will ultimately accelerate the adoption of the presented, and future wearable sensors for mHealth applications.

References

1 B. H. Dobkin, *Curr. Opin. Neurol.*, 2013, **26**, 602–8.

2 K. Takei, W. Honda, S. Harada, T. Arie and S. Akita, *Adv. Healthc. Mater.*, 2015, 487–500.

3 A. Pantelopoulos and N. G. Bourbakis, *IEEE Trans. Syst. man, Cybern. part C*, 2010, **40**, 1–12.

4 M. Chan, D. Estève, J. Fourniols, C. Escriba and E. Campo, *Artif. Intell. Med.*, 2012, **56**, 137–156.

5 Y.-L. Hsu, P.-C. Chung, W. Wei-Hsin, M.-C. Pai, W. Chun-Yao, C.-W. Lin, W. Hao-Li and W. Jeen-Shing, *IEEE J. Biomed. Heal. informatics*, 2014, **18**, 1822–1830.

6 J. P. Dieffenderfer, H. Goodell, E. Beppler, R. Jayakumar, J. S. Jur and A. Bozkurt, in *IEEE Body Sensor Networks*, 2015, pp. 1–6.

7 B. Boashash, M. S. Khlif, T. Ben-Jabeur, C. E. East and P. B. Colditz, *Digit. Signal Process.*, 2014, **25**, 134–155.

8 C.-C. Yang and Y.-L. Hsu, *Sensors (Basel).*, 2010, **10**, 7772–88.

9 S. C. Mukhopadhyay, *IEEE Sensors*, 2015, **15**, 1321–1330.

10 I. Byun, A. W. Coleman and B. Kim, *J. Micromechanics Microengineering*, 2013, **23**, 085016.

11 C. F. Guo, T. Sun, Q. Liu, Z. Suo and Z. Ren, *Nat. Commun.*, 2014, **5**, 3121.

12 D. Kang, P. V Pikhitsa, Y. W. Choi, C. Lee, S. S. Shin, L. Piao, B. Park, K.-Y. Suh, T. Kim and M. Choi, *Nature*, 2014, **516**, 222–6.

13 J. Kim, S. Park, T. Nguyen, M. Chu, J. D. Pegan and M. Khine, *Appl. Phys. Lett.*, 2016, **108**, 061901.

14 S. P. Lacour, D. Chan, S. Wagner, T. Li and Z. Suo, *Appl. Phys. Lett.*, 2006, **88**, 204103.

15 T. Li, Z. Huang, Z. Suo, S. P. Lacour and S. Wagner, *Appl. Phys. Lett.*, 2004, **85**, 3435.

16 N. Lu, X. Wang, Z. Suo and J. Vlassak, *Appl. Phys. Lett.*, 2007, **91**, 221909.

17 M. Amjadi, Y. J. Yoon and I. Park, *Nanotechnology*, 2015, **26**, 375501.

18 J. Kuang, L. Liu, Y. Gao, D. Zhou, Z. Chen, B. Han and Z. Zhang, *Nanoscale*, 2013, **5**, 12171–7.

19 X. Li, R. Zhang, W. Yu, K. Wang, J. Wei, D. Wu, A. Cao, Z. Li, Y. Cheng, Q. Zheng, R. S. Ruoff and H. Zhu, *Sci. Rep.*, 2012, **2**, 870.

20 S.-J. Park, J. Kim, M. Chu and M. Khine, *Adv. Mater. Technol.*, 2016.

21 S. Ryu, P. Lee, J. B. Chou, R. Xu, R. Zhao, A. J. Hart and S. Kim, *ACS Nano*, 2015, 5929–5936.

22 Y. Wang, R. Yang, Z. Shi, L. Zhang, D. Zhi, E. Wang and G. Zhang, *ACS Nano*, 2011, **5**, 3645–3650.

23 T. Yamada, Y. Hayamizu, Y. Yamamoto, Y. Yomogida, A. Izadi-Najafabadi, D. N. Futaba and K. Hata, *Nat. Nanotechnol.*, 2011, **6**, 296–301.

24 C. Yan, J. Wang, W. Kang, M. Cui, X. Wang, C. Y. Foo, K. J. Chee and P. S. Lee, *Adv. Mater.*, 2014, **26**, 2022–7.

25 D. W. H. Fam, A. Palaniappan, a. I. Y. Tok, B. Liedberg and S. M. Moochhala, *Sensors Actuators B Chem.*, 2011, **157**, 1–7.

26 S. Adibi, *Mobile Health: A Technology Road Map*, Springer, Switzerland, 2015.

27 R. T. Li, S. R. Kling, M. J. Salata, S. a. Cupp, J. Sheehan and J. E. Voos, *Sport. Heal. A Multidiscip. Approach*, 2016, **8**, 74–78.

28 D.-H. Kim, N. Lu, R. Ma, Y.-S. Kim, R.-H. Kim, S. Wang, J. Wu, S. M. Won, H. Tao, A. Islam, K. J. Yu, T. Kim, R. Chowdhury, M. Ying, L. Xu, M. Li, H.-J. Chung, H. Keum, M. McCormick, P. Liu, Y.-W. Zhang, F. G. Omenetto, Y. Huang, T. Coleman and J. A. Rogers, *Science (80-.).*, 2011, **333**, 838 LP – 843.

29 P. Yager, G. J. Domingo and J. Gerdes, *Annu. Rev. Biomed. Eng.*, 2008, **10**, 107–44.

30 M. Mesbah, M. S. Khlif, C. East, J. Smeathers, P. Colditz and B. Boashash, *IEEE EMBS*, 2011, 7877–7880.

31 P. Chung, C. Wang, C. Lin and J. Wang, *IEEE*, 2012, 1323–1326.

32 A. Mannini, A. M. Sabatini and S. S. Intille, *Pervasive Mob. Comput.*, 2015, **21**, 62–74.

33 J. a Rogers, T. Someya and Y. Huang, *Science*, 2010, **327**, 1603–7.

34 K. Jain, M. Klosner and M. Zemel, *Proc. IEEE*, 2005, **93**.

35 S. Hardt, *Nanosci. Technol. Inst.*, 2005, **1**, 567–570.

36 S. Lin, E. K. Lee, N. Nguyen and M. Khine, *Lab Chip*, 2014, **14**, 3475–88.

37 D. Nguyen, J. McLane, V. Lew, J. Pegan and M. Khine, *Biomicrofluidics*, 2011, **5**, 22209.

38 D. Nguyen, D. Taylor, K. Qian, N. Norouzi, J. Rasmussen, S. Botzet, M. Lehmann, K. Halverson and M. Khine, *Lab Chip*, 2010, **10**, 1623–6.

39 A. Grimes, D. N. Breslauer, M. Long, J. Pegan, L. P. Lee and M. Khine, *Lab Chip*, 2008, **8**, 170–172.

40 D. Nguyen, S. Sa, J. D. Pegan, B. Rich, G. Xiang, K. E. McCloskey, J. O. Manilay and M. Khine, *Lab Chip*, 2009, **9**, 3338–44.

41 L. R. Freschauf, J. McLane, H. Sharma and M. Khine, *PLoS One*, 2012, **7**, e40987.

42 S. Jayadev, J. Pegan, D. Dyer, J. McLane, J. Lim and M. Khine, *Smart Mater. Struct.*, 2013, **22**, 014014.

43 J. McLane, C. Wu and M. Khine, *Adv. Mater. Interfaces*, 2015, **2**, 1400034.

44 A. Chen, D. K. Lieu, L. Freschauf, V. Lew, H. Sharma, J. Wang, D. Nguyen, I. Karakikes, R. J. Hajjar, A. Gopinathan, E. Botvinick, C. C. Fowlkes, R. a Li and M. Khine, *Adv. Mater.*, 2011, **23**, 5785–91.

45 J. M. Nokes, R. Liedert, M. Y. Kim, A. Siddiqui, M. Chu, E. K. Lee and M. Khine, *Adv. Healthc. Mater.*, 2016, 1–9.

46 A. B. D. Cassie and S. Baxter, *Trans. Faraday Soc.*, 1944, **40**, 546–551.

47 C. M. Gabardo, Y. Zhu, L. Soleymani and J. M. Moran-Mirabal, *Adv. Funct. Mater.*, 2013, **23**, 3030–3039.

48 M. Leser, J. Pegan, M. El Makkaoui, J. C. Schlatterer, M. Khine, M. Law and M. Brenowitz, *Lab Chip*, 2015, **15**, 1646–1650.

49 J. D. Pegan, A. Y. Ho, M. Bachman and M. Khine, *Lab Chip*, 2013, **13**, 4205–9.

50 S. Lin, H. Sharma and M. Khine, *Adv. Opt. Mater.*, 2013, **1**, 568–572.

51 H. Sharma, J. B. Wood, S. Lin, R. M. Corn and M. Khine, *Langmuir*, 2014, **30**, 10979–83.

52 M. Madou, *Madou, Fundamentals of Microfabrication: The Science of Miniaturization, 2nd. ed.*, Taylor & Francis Group, Boca Raton, 2012.

53 S. Nonogaki, T. Ueno and T. Ito, *Microlithography Fundamentals in Semiconductor Devices and Fabrication Technology*, Marcel Dekker, New York, 1998.

54 N. Lu, C. Lu, S. Yang and J. Rogers, *Adv. Funct. Mater.*, 2012, **22**, 4044–4050.

55 P. S. Ho, R. Haight, R. C. White, B. D. Silverman and F. Faupel, in *Fundamentals of Adhesion*, ed. L. H. Lee, Springer US, New York, 1st edn., 1991, p. 425.

56 F. D. Egitto and L. J. Matienzo, *IBM J. Res. Dev.*, 1994, 38, 423–439.

57 N. Bowden, S. Brittain, A. G. Evans, J. W. Hutchinson and G. M. Whitesides, *Nature*, 1998, **393**, 146–149.

58 J. S. Mijovic and J. A. Koutsky, *Polym. Plast. Technol. Eng.*, 1977, **9**, 139–179.

59 M. Urdea, L. a Penny, S. S. Olmsted, M. Y. Giovanni, P. Kaspar, A. Shepherd, P. Wilson, C. a Dahl, S. Buchsbaum, G. Moeller and D. C. Hay Burgess, *Nature*, 2006, **444**, 73–9.

60 H. Sharma, D. Nguyen, A. Chen, V. Lew and M. Khine, *Ann. Biomed. Eng.*, 2011, **39**, 1313–27.

61 C. D. Chin, T. Laksanasopin, Y. K. Cheung, D. Steinmiller, V. Linder, H. Parsa, J. Wang, H. Moore, R. Rouse, G. Umviligihozo, E. Karita, L. Mwambarangwe, S. L. Braunstein, J. van de Wijgert, R. Sahabo, J. E. Justman, W. El-Sadr and S. K. Sia, *Nat. Med.*, 2011, **17**, 1015–9.

62 C. D. Chin, V. Linder and S. K. Sia, *Lab Chip*, 2012, **12**, 2118–34.

63 X. Li, D. R. Ballerini and W. Shen, *Biomicrofluidics*, 2012, **6**, 11301–1130113.

64 L. Ge, J. Yan, X. Song, M. Yan, S. Ge and J. Yu, *Biomaterials*, 2012, **33**, 1024–31.

65 C. Qiu, X. Wang, X. Liu, S. Hou and H. Ma, *Electrochim. Acta*, 2012, **67**, 140–146.

66 N. J. Ronkainen, H. B. Halsall and W. R. Heineman, *Chem. Soc. Rev.*, 2010, **39**, 1747–63.

67 C.-L. Sun, H.-H. Lee, J.-M. Yang and C.-C. Wu, *Biosens. Bioelectron.*, 2011, **26**, 3450–5.

68 M. Venugopal, S. K. Arya, G. Chornokur and S. Bhansali, *Sensors Actuators A Phys.*, 2011, **172**, 154–160.

69 H. Wei and E. Wang, *Luminescence*, 2011, **26**, 77–85.

70 Y. Yuan, S. Han, L. Hu, S. Parveen and G. Xu, *Electrochim. Acta*, 2012, **82**, 484–492.

71 E. J. O'Reilly, T. E. Keyes, R. J. Forster and L. Dennany, *Analyst*, 2013, **138**, 677–82.

72 J. L. Delaney, C. F. Hogan, J. Tian and W. Shen, *Anal. Chem.*, 2011, **83**, 1300–6.

73 N. P. Sardesai, K. Kadimisetty, R. Faria and J. F. Rusling, *Anal. Bioanal. Chem.*, 2013, **405**, 3831–8.

74 D. Nawarathna, N. Norouzi, J. McLane, H. Sharma, N. Sharac, T. Grant, A. Chen, S. Strayer, R. Ragan and M. Khine, *Appl. Phys. Lett.*, 2013, **102**, 63504.

75 D. Taylor, D. Dyer, V. Lew and M. Khine, *Lab Chip*, 2010, **10**, 2472–5.

76 H. Sharma, D. Nguyen, A. Chen, V. Lew and M. Khine, *Ann. Biomed. Eng.*, 2011, **39**, 1313–27.

77 F. Greco, L. Ventrelli, P. Dario, B. Mazzolai and V. Mattoli, *Int. J. Hydrogen Energy*, 2012, **37**, 17529–17539.

78 L. Soleymani, Z. Fang, E. H. Sargent and S. O. Kelley, *Nat. Nanotechnol.*, 2009, **4**, 844–8.

79 K. B. Cederquist and S. O. Kelley, *Curr. Opin. Chem. Biol.*, 2012, **16**, 415–21.

80 L. Xue, L. Guo, B. Qiu, Z. Lin and G. Chen, *Electrochem. commun.*, 2009, **11**, 1579–1582.

81 C. a Schneider, W. S. Rasband and K. W. Eliceiri, *Nat. Methods*, 2012, **9**, 671–675.

82 K. L. Chopra, L. C. Bobb and M. H. Francombe, 1963, **100**, 4–7.

83 X. Liu, Y. Zhu, M. W. Nomani, X. Wen, T.-Y. Hsia and G. Koley, *J. Micromechanics Microengineering*, 2013, **23**, 025022.

84 R. Li, B. Nie, C. Zhai, J. Cao, J. Pan, Y.-W. Chi and T. Pan, *Ann. Biomed. Eng.*, 2016, **44**, 2282–2291.

85 S. Gong, W. Schwalb, Y. Wang, Y. Chen, Y. Tang, J. Si, B. Shirinzadeh and W. Cheng, *Nat. Commun.*, 2014, **5**, 1–8.

86 Y. Wang, L. Wang, T. Yang, X. Li, X. Zang, M. Zhu, K. Wang, D. Wu and H. Zhu, *Adv. Funct. Mater.*, 2014, **24**, 4666–4670.

87 M. Zens, P. Niemeyer, A. Bernstein, M. J. Feucht, J. Kühle, N. P. Südkamp, P. Woias and H. O. Mayr, *Knee surgery, Sport. Traumatol. Arthrosc.*, 2015, **23**, 2868–75.

88 S. Patel, H. Park, P. Bonato, L. Chan and M. Rodgers, *J. Neuroeng. Rehabil.*, 2012, **9**, 1–17.

89 H. Cong and T. Pan, *Adv. Funct. Mater.*, 2008, **18**, 1912–1921.

90 R. Zhang, K. Moon, W. Lin, J. C. Agar and C. Wong, *Compos. Sci. Technol.*, 2011, **71**, 528–534.

91 A. R. Madaria, A. Kumar, F. N. Ishikawa and C. Zhou, *Nano Res.*, 2010, 564–573.

92 J. Van Den Brand, M. De Kok, M. Koetse, M. Cauwe, R. Verplancke, F. Bossuyt, M. Jablonski and J. Vanfleteren, *Solid State Electron.*, 2015, **113**, 116–120.

93 Z. Nie, C. a Nijhuis, J. Gong, X. Chen, A. Kumachev, A. W. Martinez, M. Narovlyansky and G. M. Whitesides, *Lab Chip*, 2010, **10**, 477–83.

94 L. Li, Y. Shi, L. Pan, Y. Shi and G. Yu, *J. Mater. Chem. B*, 2015, **3**, 2920–2930.

95 L. Li, Y. Wang, L. Pan, Y. Shi, W. Cheng, Y. Shi and G. Yu, *Nano Lett.*, 2015, **15**, 1146–51.

96 L. Pan, A. Chortos, G. Yu, Y. Wang, S. Isaacson, R. Allen, Y. Shi, R. Dauskardt and Z. Bao, *Nat. Commun.*, 2014, **5**, 3002.

97 J. a Fan, W.-H. Yeo, Y. Su, Y. Hattori, W. Lee, S.-Y. Jung, Y. Zhang, Z. Liu, H. Cheng, L. Falgout, M. Bajema, T. Coleman, D. Gregoire, R. J. Larsen, Y. Huang and J. a Rogers, *Nat. Commun.*, 2014, **5**, 3266.

98 M. Li, H. Li, W. Zhong, Q. Zhao and D. Wang, *ACS Appl. Mater. Interfaces*, 2014, **6**, 1313–1319.

99 X. Liao, Q. Liao, X. Yan, Q. Liang, H. Si, M. Li, H. Wu, S. Cao and Y. Zhang, *Adv. Funct. Mater.*, 2015, **25**, 2395–2401.

100 K. Yong, A. Ashraf, P. Kang and S. Nam, *Sci. Rep.*, 2016, **6**, 24890.

101 Y. Arafat, I. Dutta and R. Panat, *Appl. Phys. Lett.*, 2015, **107**, 081906.

102 Y. Hsu, M. Gonzalez, F. Bossuyt, J. Vanfleteren, I. De Wolf and S. Member, *IEEE Trans. Electron Devices*, 2011, **58**, 2680–2688.

103 N. Lu, Z. Suo and J. J. Vlassak, *Acta Mater.*, 2010, **58**, 1679–1687.

104 M. C. Salvadori, I. G. Brown, a. R. Vaz, L. L. Melo and M. Cattani, *Phys. Rev. B*, 2003, **67**, 153404.

105 Y. Huang, Y. Wang, L. Xiao, H. Liu, W. Dong and Z. Yin, *Lab Chip*, 2014, **14**, 4205–12.

106 H. Liu, L. Zhang, X. Lang, Y. Yamaguchi, H. Iwasaki, Y. Inouye, Q. Xue and M. Chen, *Sci. Rep.*, 2011, **1**, 112.

107 L. Zhang, X. Lang, A. Hirata and M. Chen, *ACS Nano*, 2011, 4407–4413.

108 S. M. Woo, C. M. Gabardo and L. Soleymani, *Anal. Bioanal. Chem.*, 2014, **86**, 12341–12347.

109 T. Li, Z. Y. Huang, Z. C. Xi, S. P. Lacour, S. Wagner and Z. Suo, *Mech. Mater.*, 2005, **37**, 261–273.

110 T. Kondo, T. Uhlig, P. Pemberton and P. D. Sly, *Eur. Respir. J.*, 1997, **10**, 1865–1869.

111 G. J. Tammeling and O. F. Pedersen, *Eur. Respir. J.*, 1993, **6**, 5–40.

112 K. Konno and J. Mead, *J. Appl. Physiol.*, 1967, **22**, 407–422.

113 J. D. Pegan, J. Zhang, M. Chu, T. Nguyen, S.-J. Park, A. Paul, J. Kim, M. Bachman and M. Khine, *Nanoscale*, 2016, **8**, 17295–17303.

114 S.-H. Bae, Y. Lee, B. K. Sharma, H.-J. Lee, J.-H. Kim and J.-H. Ahn, *Carbon N. Y.*, 2013, **51**, 236–242.

115 J. Lee, S. Kim, J. Lee, D. Yang, B. C. Park, S. Ryu and I. Park, *Nanoscale*, 2014, **6**, 11932–11939.

116 Y. Zhu and J. Moran-Mirabal, *Adv. Electron. Mater.*, 2016, **2**, n/a–n/a.

117 A. L. Window and G. S. Holister, *Strain gauge technology.*, Applied science publishers, 1982.

118 V. Linder, B. D. Gates, D. Ryan, B. a Parviz and G. M. Whitesides, *Small*, 2005, **1**, 730–6.